Distinguishing Relative Aqueous Alteration and Heating among CM Chondrites with IR Spectroscopy

R.D. Hanna[a,*], V.E. Hamilton[b], C.W. Haberle[c], A.J. King[d], N.M. Abreu[e], J.M. Friedrich[f,g]

[a]Jackson School of Geosciences, University of Texas at Austin, Austin TX, 78712, USA, romy@jsg.utexas.edu

[b]Department of Space Studies, Southwest Research Institute, Boulder, CO, 80302, USA

[c]School of Earth and Space Exploration, Arizona State University, Tempe, AZ, 85287, USA

[d]School of Physical Sciences, The Open University, Walton Hall, Milton Keynes MK7 6AA, UK

[e]Earth Science Program, Pennsylvania State University, Du Bois, PA 15801, USA

[f]Department of Chemistry, Fordham University, Bronx, NY 10458, USA

[g]Department of Earth and Planetary Sciences, American Museum of Natural History, New York, NY 10024, USA

[*]Corresponding author

Abstract

Using infrared (IR) spectroscopy of thin sections, we characterize the relative degree of aqueous alteration and subsequent heating of a suite of CM chondrites to document spectral indicators of these processes that can contextualize observations of carbonaceous asteroids. We find that IR spectroscopy reveals the subtle progressive alteration of the CMs in two different ways. The low-wavenumber region (1200–400 cm^{-1}; 8–25 μm) records the increasing proportion of Mg-Fe phyllosilicates relative to anhydrous silicates as aqueous alteration proceeds, with a highly correlated shift of the Christiansen feature (CF) to lower wavenumber and the Si-O bending band minimum to higher wavenumber, and an increase in depth of the Mg-OH band (~625 cm^{-1}). The strongest correlation (R^2=0.90) with petrologic subtype is the distance between the CF and Si-O stretching minimum, which predicts the petrologic subtype of the sample to within 0.1. The high-wavenumber region (4000–2500 cm^{-1}; ≤3.33 μm) probes the variation in abundance and composition of Mg-Fe serpentine and tochilinite among the altered CMs. All moderately to highly altered CMs (≤ 2.3) have an OH/H_2O band emission maximum of 3690 cm^{-1} (2.71 μm) indicative of Mg-bearing serpentine, and mildly aqueously altered CMs (≥ 2.5) have a wider band with a complex shape that results from contributions of Fe-bearing serpentine and tochilinite. Among weakly heated CMs, the low-wavenumber region exhibits spectral features resulting from the dehydration and dehydroxylation of phyllosilicates that include broadening of the Si-O stretching band and a shift of its minimum to lower wavenumber, and the disappearance of the Mg-OH band. The location of the Si-O bending band minimum appears to be unaffected by mild heating. Among extensively heated CMs, the low-wavenumber region is dominated by the spectral features of secondary, Fe-bearing olivine and low-Ca pyroxene. The OH/H_2O band of all heated CMs is broad and rounded with an emission peak at

higher wavenumbers (≤ 3636 cm^{-1}; ≥ 2.75 μm) than in unheated CMs. However, spectral and petrographic evidence suggests that our heated CMs have been compromised by terrestrial rehydration. Our study confirms that thermal metamorphism effects are concentrated within the matrix and suggests that the matrix of the CM WIS 91600 had a CI-like mineralogy prior to heating.

Keywords: spectroscopy; meteorites; geological processes; asteroids, composition

1. Introduction

The CM carbonaceous chondrites are a group of meteorites that show variation in the effects of the earliest stages of metamorphism, specifically aqueous alteration and thermal processing, through their physical and chemical characteristics. Detailed investigations of this group provide an opportunity to extract information on how and when primitive Solar System material was geologically altered from a more pristine state, and as such they have been studied in great detail. It has long been recognized that aqueous alteration of the CMs is a progressive sequence of mineralogical and chemical changes resulting in the destruction of metal and chondrule glass mesostasis, serpentinization of anhydrous silicates (olivine, pyroxene), and the mobilization of Fe and Mg to form initially Fe-bearing and then Mg-rich serpentine (Tomeoka et al., 1989; Zolensky et al., 1993; Browning et al., 1996; Zolensky et al., 1997; Lauretta et al., 2000; Rubin et al., 2007; Howard et al., 2015; Leroux et al., 2015). A subset of CMs have also experienced post-aqueous alteration heating (i.e., thermal metamorphism) (e.g., Lipschutz et al., 1999; Nakamura, 2005; Tonui et al., 2014). The degree of heating experienced by a CM chondrite can be identified based on mineralogical changes, primarily the dehydration and dehydroxylation of

63 phyllosilicates and eventual formation of secondary olivine and pyroxene from phyllosilicates
64 (Lipschutz et al., 1999; Nakamura, 2005; Tonui et al., 2014), as well as the modification and
65 structural changes of organic material within it (Quirico et al., 2014; Quirico et al., 2018).
66 There has been great interest in characterizing CMs using spectroscopic methods to allow for
67 direct comparison of their spectra to those of asteroids from telescopic and spacecraft data (e.g.,
68 Gaffey, 1976; Hiroi et al., 1996; Sato et al., 1997). More recent efforts have endeavored to relate
69 the spectral signatures of CMs to their degree of aqueous alteration or heating to more accurately
70 interpret the spectra of C-complex asteroids, which may host CM or CM-like material (Gaffey et
71 al., 1993a; Beck et al., 2010; Cloutis et al., 2011; Cloutis et al., 2012; Takir et al., 2013; Beck et
72 al., 2014; McAdam et al., 2015; Garenne et al., 2016; Beck et al., 2018). Data acquisition and
73 sample preparation methods among these previous studies have varied, and in some cases their
74 applicability to ground- or spacecraft-based spectral observations is limited. First, these studies
75 collected spectral data of particulate samples that were ground from meteorite chips. This
76 complicates the comparison of the laboratory data to asteroid observations as particle size effects
77 can substantially modify the depth, shape, and/or position of spectral bands in the IR (e.g., Lyon,
78 1964; Salisbury, 1993). Further, IR spectra of silicates with fine particle sizes (<75 μm) display
79 scattering (transparency) features in wavelength regions where their absorption coefficients are
80 extremely low (e.g., Vincent and Hunt, 1968; Salisbury and Walter, 1989), and the recent arrival
81 of spacecraft to carbonaceous asteroids (162173) Ryugu and (101955) Bennu has revealed that
82 their regolith is dominated by coarse particulates and rocks (Hamilton et al., 2019; Okada et al.,
83 2019). In addition, the petrographic context of the material is lost other than the general 'bulk
84 composition' of the stone that was ground. Another complication of grinding CM chondrites in
85 the laboratory is contamination of the powders with adsorbed terrestrial water, which modifies

the shape and position of the "3-μm" water band (referred to as the OH/H_2O band in the remainder of the manuscript) that is diagnostic of hydrated minerals within CM chondrites (Beck et al., 2010; Takir et al., 2013). Many spectral studies have heated chondrite powders to minimize this effect, but it is unclear if all terrestrial adsorbed water is being removed and whether heating could be modifying the native water band through thermal modification of the phyllosilicate or hydrated Fe sulfide (tochilinite), the latter of which breaks down at temperatures as low as 120°C (Fuchs et al., 1973; Zolensky et al., 1997). Finally, grinding of phyllosilicates [which are the dominant mineralogy in CMs (Howard et al., 2009)] in the laboratory has been shown to damage their structure and change their spectral character (e.g., Drief and Nieto, 1999).

The Origins, Spectral Interpretation, Resource Identification, and Security–Regolith Explorer (OSIRIS-REx) mission to asteroid (101955) Bennu is equipped with the OSIRIS-REx Thermal Emission Spectrometer (OTES) that collects spectra in the 1750–100 cm^{-1} wavenumber region (5.71–100 μm) (Christensen et al., 2018). Because OTES is measuring emitted energy, previous spectral studies that have collected IR data of CM chondrites in transmission (Beck et al., 2010; Beck et al., 2014) or bidirectional reflectance (Beck et al., 2018) are not directly applicable to OTES measurements. Although McAdam et al. (2015) collected bi-conical reflectance of CMs [which are equivalent to emissivity through Kirchhoff's Law (Salisbury, 1993)], the samples were powdered (~35 μm) and the spectra are dominated by transparency features. Other recent IR emission and diffuse reflectance studies of CM and CI chondrites are likewise dominated by transparency features due to fine particle sizes (Donaldson Hanna et al., 2019; Bates et al., 2020) thereby complicating direct comparison to some asteroid regolith surfaces such as Ryugu and Bennu that do not appear to contain abundant fine-grained material (DellaGiustina et al., 2019; Grott et al., 2019). Initial results from the OSIRIS-REx mission indicate that Bennu's surface is

dominated by a hydrous mineralogy consistent with a low petrologic type-2 CM lithology, and the average OTES spectrum does not show strong transparency features attributable to fine-particulate silicates (Hamilton et al., 2019).

The primary goal of our study is to identify IR spectral trends that are correlated with degree of aqueous alteration and heating among CM chondrites. Ultimately, the knowledge gained from these laboratory-based observations will be used to remotely characterize aqueous alteration and possible heating of CM material on Bennu from OTES and OSIRIS-REx Visible and InfraRed Spectrometer (OVIRS) data. We anticipate that our results also will be useful in the investigation of other asteroids that may have CM material on their surfaces, as well as for rapid characterization of CMs in the laboratory using bulk samples or thin sections. We do not aim to relate spectral features to modal mineral abundances or specific chemical compositions of minerals within CMs [which can vary within a petrologic subtype (Rubin et al., 2007; Howard et al., 2015)]; rather, we identify broad spectral trends that are correlated with mineralogical and compositional changes resulting from aqueous alteration and heating. Additionally, microscopic Fourier transform infrared (μ-FTIR) spectroscopy, which can collect spectral data of samples mounted in thin section, provides an in situ view of spectral trends while retaining spatial context, allowing insights into the details of aqueous alteration and heating within CM chondrites. Both topics will be explored in this paper.

2. Methods

2.1 Samples

We analyzed 13 CMs that represent a range of aqueous alteration [2.0–2.7 on the Rubin et al. (2007) scale] and degree of heating [Stages II–III/IV; (Nakamura, 2005)], as well as one CI

(Alais) to use as a comparison to the most altered CMs (Tables 1–2). While some isotopic data suggest that WIS 91600 may be better classified as an ungrouped carbonaceous chondrite rather than a CM (Alexander et al., 2007; Yabuta et al., 2010; Tonui et al., 2014), we include it here as the latter but explore this classification issue in the discussion section. All samples apart from Murchison and Alais are Antarctic finds. Five of the unheated CMs (LAP 04514, LAP 02333,

Table 1. Altered CMs and CI examined for this study

	Section number	Petrologic subtype[a]	Weathering grade	PSF[b]	Alteration Index[c]	Equivalent Petrologic Subtype[d]	Olivine (vol%)	Pyroxene (vol%)	Magnetite (vol%)	Fe-sulfide (vol%)	Calcite (vol%)	Gypsum (vol%)	FeNi metal (vol%)	Fe-rich phyllosilicate (vol%)	Mg-rich phyllosilicate (vol%)	Total (vol%)	Petrologic Subtype Reference	PSD-XRD Data Reference
LAP 04514	6	2.7	B	0.74	1.6	2.5	10.9	14.2	2.3	1.3	0.9	0.0	0.0	42.8	27.4	99.8	e	f
LAP 02333[j]	2	2.6	B	0.73	1.5	2.4	9.6	10.2	1.9	1.2	0.95	0	0	23.6	52.5	100.0	e	g, f
Murchison	USNM 5487-3, USNM 5487-1	2.5	n.a.	0.49	1.5	2.4	15.1	8.3	1.1	1.8	1.2	0.0	0.0	50.3	22.2	100.0	a	g
LAP 031214	7	2.3	B	0.63	1.6	2.5	18.2	5.9	2.3	1.1	1.0	0.3	0.0	30.8	40.4	100.0	e	h
LEW 90500	60	2.2	B	0.67	1.5	2.4	15.2	4.9	1.9	3.1	1.0	3.7	0.0	27.7	41.7	99.2	e	g
ALH 85013	13	2.2	A	0.76	1.3	2.2	9.8	3.4	1.6	1.6	4.0	1.9	0.0	37.1	40.7	100.1	e	g
LAP 031166	16	2.1	B	0.91	1.2	2.1	5.0	1.5	2.0	1.4	0.9	2.4	0.0	21.5	65.3	100.0	e	h
LAP 02277	38	2.0	A	0.93	1.2	2.1	5.3	0.0	1.9	2.2	1.7	0.0	0.0	20.6	68.3	100.0	a, e	h
CI Alais	P10910	n.a.	n.a.	1.00	n.a.	n.a.	0.0	0.0	7.0	4.0	3.0	0.0	0.0	0.0	83.0	97.0	n.a.	i

[a]Rubin et al. (2007) scale
[b]PSF of g calculated from XRD values in this table
[c]From PSF of this work
[d]Using Equation (2) of g
[e]Friedrich et al. (2018)
[f]Mason et al. (2018)
[g]Howard et al. (2015)
[h]King et al. (2017)
[i]King et al. (2015)
[j]PSD-XRD data average of g and f

Table 2. Heated CMs examined for this study

	Section number	Sample number for PSD-XRD	Heating Stage[a]	Weathering grade	Olivine (vol%)	Pyroxene (vol%)	Magnetite (vol%)	Fe-sulfide (vol%)	Calcite (vol%)	Gypsum (vol%)	FeNi metal (vol%)	"Rusts" (vol%)	Feldspar (vol%)	Fe-rich Phyllosilicate (X-ray amorphous) (vol%)	Mg-rich Phyllosilicate (X-ray amorphous) (vol%)	Total (vol%)	Decomposed/ Dehydrated Phyllosilicate	Secondary Olivine	Heating Stage Reference
WIS 91600[b]	22	76,9	II	A/B	10.1	1.5	7.8	3.7	0.6	0.0	0.0	0.0	0.0	3.8	74.4	101.7	yes	no	c, d, e
EET 87522	30	51, 2	II	Be	*15.3*	*6.6*	*1.9*	*0.7*	*0.4*	*0.2*	*0.1*	*0.0*	*0.0*	*34.8*	*40.0*	*100.0*	yes	no	c, e
EET 96029	23	57, 21[g]	II	A/B	12.2	15.7	3.1	2.4	1.0	1.0	0.3	0.0	0.0	24.7	40.0	100.4	yes	no	c, g
PCA 91008	6	37, 5	III	B/C	*76.7*	*16.9*	*2.5*	*0.8*	*0.0*	*2.7*	*0.0*	*0.4*	*0.0*	*0.0*	*0.0*	*100.0*	*yes*	*yes*	c, d, e, a, h
PCA 02010	11	24, 2	III/IV	B	*75.2*	*16.1*	*0.0*	*3.8*	*1.3*	*0.0*	*0.4*	*0.0*	*3.2*	*0.0*	*0.0*	*100.0*	*yes*	*yes*	f, h, i

Italics: This work

[a]Nakamura (2005) scale

[b]PSF XRD data average of Howard et al. (2015) and this work, sample number refers to this work [Howard et. al (2015) reported 73.5% Mg-rich phyllosilicate as crystalline for their sample]

[c]Quirico et al. (2018)

[d]Tonui et al. (2014)

[e]Nakato et al. (2009)

[f]Garenne et al. (2014)

[g]PSD-XRD from Lee et al. (2016)

[h]Beck et al. (2014)

[i]Alexander et al. (2013)

LAP 031214, LAP 031166, ALH 85013) are the same sample sections analyzed by Friedrich et al. (2018), and the two Murchison sections are from the sample analyzed and described in Hanna et al. (2015). Two samples with the same petrologic subtype (2.2; ALH 85013 and LEW 90500) were selected to examine intra-subtype variability in the μ-FTIR spectra. In all cases, the same sample section was used for both μ-FTIR spectroscopy and electron microscopy. For the Antarctic finds, all samples are weathering grade A, A/B, or B (apart from PCA 91008, which has been assigned a B/C) (Table 1), indicating minor to moderate terrestrial weathering of the samples. We checked all sections for indications of terrestrial weathering [rust, evaporites, sulfate or carbonate veins (Bland et al., 2006)] and noted weathering effects where apparent below. In addition, we determined the modal mineralogy of separate aliquots of the heated CM chondrites WIS 91600, EET 87522, PCA 91008, and PCA 02010 using position sensitive detector X-ray diffraction (PSD-XRD) to verify the previously assigned heating stage and check for terrestrial weathering products (Table 2).

2.2 Electron microscopy

We used scanning electron microscopy (SEM) to provide mineralogical and textural context for the μ-FTIR spectra and to verify the relative degree of alteration and heating among the CM samples. For the five CM sections previously analyzed by Friedrich et al. (2018), the backscattered electron (BSE) image and energy dispersive (EDS) X-ray data collection are described in that work. Likewise, BSE imagery and EDS analysis of the Murchison sections are described in Hanna et al. (2015). For the five heated CMs (Table 2) and the unheated CM LEW 90500, we collected whole-section BSE and EDS mosaics on a FEI XL 30 ESEM at the Electron Microbeam Analysis Laboratory at the Jackson School of Geosciences at the University of Texas

(UT) at Austin. Sections were not carbon-coated, thus all data collection was done at low pressure (0.1 Torr) with H_2O gas with a 20.0 kV beam and a working distance that varied slightly per session (9.9–10.1 mm). EDS X-ray elemental maps were generated using major element Kα peaks. For LAP 02277, we collected whole-section BSE and wavelength dispersive (WDS) X-ray mosaics on a JEOL JXA-8200 Electron Microprobe (EPMA) at the same UT facility. The section was carbon-coated, and data were collected at 15 kV and 38 mA with a dwell time of 4 ms (focused beam). We collected all BSE, EDS, and WDS data after IR reflectance measurements.

2.3 *PSD-XRD analysis*

Meteorite chips (~50 mg) were powdered using an agate mortar and pestle, then analyzed using an INEL XRD equipped with a curved 120° PSD at the Natural History Museum, London. XRD patterns were collected for 16 hours from the meteorite samples and for 30 minutes from standards of all minerals present in the meteorites. Differences in the incident beam flux throughout the experimental run were monitored by analyzing a polished block of Fe metal at the start of each day.

Mineral abundances were determined using a profile-stripping method that has previously been applied to both unheated and heated CM chondrites (e.g. Howard et al., 2015; King et al., 2015). The XRD pattern of a mineral standard was scaled to the same length of time as the meteorite analyses (i.e. ×32), then reduced in intensity by a factor to match its intensity in the XRD pattern of the meteorite sample. The standard pattern was subtracted to leave a residual meteorite pattern, and this process was repeated for all phases identified in the meteorite until there were zero counts left in the residual and the sum of the fit factors was one. The fit factors

for the mineral standards were then corrected for relative differences in X-ray absorption to give a final volume fraction in the meteorite. Uncertainties on the measured abundances are 2–4% for crystalline anhydrous phases and 3–5% for fine-grained, poorly crystalline phyllosilicates.

2.4 μ-FTIR

We collected IR reflectance spectra (4000–400 cm^{-1}, 2.5–25 μm) of all samples with a Thermo Scientific iN10 FTIR microscope (μ-FTIR) equipped with an extended range, liquid nitrogen–cooled mercury cadmium telluride (MCT) detector, and potassium bromide (KBr) beamsplitter. Samples were mounted as polished thin sections (no carbon coat), and individual spectra were acquired as the average of 256 scans at a spatial resolution of 300 μm per pixel and spectral sampling of 2 cm^{-1}. Except as noted below, all data were collected as maps using the attached, automated sample stage. Collected map sizes for each sample are reported in Tables 3 and 4. Measured radiance was converted to biconical reflectance using a polished gold plate mounted on the stage as the background. A background was collected every 15–30 minutes during mapping to account for any variability in atmospheric conditions or instrument drift over time. Because the spectrometer has a permanently aligned, 15X 0.7 N.A. (half angle range 20° to 43.5°) visible/IR objective and condenser, the solid angle is sufficiently small that band-broadening effects, typically associated with biconical reflectance systems, are not observed (Hamilton, 2018). Therefore the reflectance spectra have equivalence with emission and are converted to emissivity using Kirchhoff's Law $E = 1 - R$, where E is the emissivity and R is the reflectance (Salisbury, 1993). This conversion enables a more direct comparison of our laboratory data to IR emissivity datasets from instruments such as OTES (Christensen et al., 2018).

Table 3. Altered CMs and CI spectral parameters

	Petrologic subtype[a]	Sample area for µFTIR (x90000 µm^2)	Christiansen feature (cm^{-1})	Si-O stretching band minimum (cm^{-1})	Separation of CF and Si-O stretching band minimum (cm^{-1})	Si-O stretching band symmetry	Mg-OH band minimum (cm^{-1})	Mg-OH band depth	Si-O bending band minimum (cm^{-1})	OH/H_2O band maximum (cm^{-1})	OH/H_2O band maximum (µm)	OH/H_2O band center (cm^{-1})	OH/H_2O band center (µm)	OH/H_2O band depth
LAP 04514	2.7	532	1155	948 (2)	207	0.95 (0.06)	619 (3)	0.0071 (0.0001)	432 (0)	3671 (2)	2.724 (0.002)	3667 (4)	2.727 (0.003)	0.0052 (0.0000)
LAP 02333	2.6	522	1176	946 (3)	231	1.01 (0.06)	615 (6)	0.0065 (0.0002)	427 (2)	3623 (1)	2.760 (0.001)	3622 (2)	2.761 (0.002)	0.0079 (0.0001)
Murchison	2.5	796	1147	944 (2)	204	0.97 (0.04)	620 (4)	0.0095 (0.0001)	430 (7)	3626 (3)	2.758 (0.002)	3643 (4)	2.745 (0.003)	0.0069 (0.0001)
LAP 031214	2.3	436	1136	959 (2)	177	0.81 (0.03)	619 (3)	0.0164 (0.0004)	438 (4)	3686 (4)	2.713 (0.003)	3661 (5)	2.731 (0.004)	0.0083 (0.0002)
LEW 90500	2.2	354	1120	952 (1)	168	0.86 (0.02)	619 (2)	0.0153 (0.0001)	442 (1)	3685 (3)	2.714 (0.002)	3679 (4)	2.718 (0.003)	0.0072 (0.0001)
ALH 85013	2.2	534	1126	966 (4)	160	0.75 (0.06)	618 (2)	0.0159 (0.0003)	440 (1)	3686 (3)	2.713 (0.003)	3665 (5)	2.729 (0.004)	0.0075 (0.0002)
LAP 031166	2.1	495	1128	984 (9)	144	0.69 (0.14)	625 (2)	0.0248 (0.0004)	446 (1)	3693 (3)	2.708 (0.002)	3693 (5)	2.708 (0.004)	0.0075 (0.0000)
LAP 02277	2.0	195	1111	970 (3)	141	0.80 (0.05)	625 (1)	0.0297 (0.0002)	442 (4)	3693 (3)	2.708 (0.002)	3693 (3)	2.708 (0.003)	0.0080 (0.0002)
CI Alais	n.a.	114	1126	1008 (2)	119	0.40 (0.03)	600 (12)	0.0131 (0.0008)	450 (2)	3691 (2)	2.710 (0.001)	3690 (7)	2.710 (0.005)	0.0061 (0.0001)
LAP 04514 matrix	2.7	11	1117	970 (3)	147	0.70 (0.05)	627 (0)	0.0127 (0.0000)	443 (3)	3671 (4)	2.724 (0.003)	3668 (6)	2.726 (0.004)	0.0066 (0.0003)
LAP 02333 matrix	2.6	10	1136	977 (2)	159	0.66 0.03)	630 (2)	0.0148 (0.0017)	441 (1)	3629 (4)	2.756 (0.003)	3626 (4)	2.758 (0.003)	0.0118 (0.0004)
Murchison matrix	2.5	16	1122	964 (2)	159	0.77 (0.03)	624 (2)	0.0167 (0.0003)	440 (4)	3628 (3)	2.756 (0.002)	3652 (3)	2.738 (0.002)	0.0084 (0.0001)
LAP 031214 matrix	2.3	11	1124	979 (5)	145	0.58 (0.07)	617 (2)	0.0186 (0.0002)	440 (1)	3686 (3)	2.713 (0.002)	3665 (5)	2.729 (0.004)	0.0097 (0.0001)
LEW 90500 matrix	2.2	12	1107	967 (3)	140	0.72 (0.03	617 (1)	0.0170 (0.0002)	445 (0)	3686 (3)	2.713 (0.002)	3684 (8)	2.714 (0.006)	0.0085 (0.0002)
ALH 85013 matrix	2.2	11	1120	984 (4)	137	0.58 (0.05)	618 (2)	0.0161 (0.0003)	444 (2)	3685 (4)	2.713 (0.003)	3679 (11)	2.718 (0.008)	0.0091 (0.0002)
LAP 031166 matrix	2.1	10	1136	993 (5)	142	0.62 (0.09)	628 (2)	0.0428 (0.0004)	448 (4)	3693 (1)	2.707 (0.001)	3692 (4)	2.709 (0.003)	0.0082 (0.0000)
LAP 02277 matrix	2.0	10	1115	970 (4)	144	0.82 (0.09)	627 (0)	0.0554 (0.0000)	445 (4)	3693 (0)	2.708 (0.000)	3693 (3)	2.708 (0.003)	0.0080 (0.0002)

2σ uncertainty in parentheses

[a]Rubin et al. (2007) scale

Table 4. Heated CMs spectral parameters

	Sample area for µFTIR (x90000 µm^2)	Christiansen feature (cm^{-1})	Si-O stretching band minimum (cm^{-1})	Separation of CF and Si-O stretching band minimum (cm^{-1})	Si-O stretching band symmetry	Si-O bending band minimum (cm^{-1})	OH/H_2O band maximum (cm^{-1})	OH/H_2O band maximum (µm)	OH/H_2O band center (cm^{-1})	OH/H_2O band center (µm)	OH/H_2O band depth
WIS 91600	534	1149	982 (7)	167	0.53 (0.07)	445 (4)	3643 (5)	2.745 (0.004)	3639 (4)	2.748 (0.003)	0.00336 (3e10^{-5})
EET 87522	441	1165	934 (4)	230	1.17 (0.08)	426 (5)	3600 (4)	2.778 (0.003)	3592 (3)	2.784 (0.002)	0.00469 (2e10^{-5})
EET 96029	330	1165	935 (4)	230	1.20 (0.08)	428 (3)	3591 (3)	2.785 (0.002)	3586 (2)	2.788 (0.002)	0.00441 (3e10^{-5})
PCA 91008	276	1184	876 (3)	308	2.00 (0.14)	*n.d.*	3529 (2)	2.834 (0.002)	3531 (1)	2.832 (0.001)	0.00520 (5e10^{-5})
PCA 02010	309	1180	878 (4)	302	1.50 (0.12)	*n.d.*	3495 (5)	2.861 (0.004)	3494 (6)	2.862 (0.005)	0.00344 (6e10^{-5})
WIS 91600 matrix	33	1146	1001 (1)	145	0.42 (0.01)	451 (2)	3651 (2)	2.739 (0.001)	3647 (3)	2.742 (0.002)	0.00405 (0e10^{-5})
EET 87522 matrix	11	1161	916 (5)	245	1.52 (0.10)	433 (5)	3593 (6)	2.783 (0.005)	3600 (3)	2.778 (0.002)	0.00623 (2e10^{-5})
EET 96029 matrix	11	1174	990 (2)	184	0.46 (0.02)	433 (7)	3617 (3)	2.765 (0.002)	3609 (2)	2.771 (0.002)	0.00671 (0e10^{-5})
PCA 91008 matrix	10	1167	873 (3)	294	1.53 (0.14)	*n.d.*	3535 (3)	2.829 (0.002)	3538 (3)	2.826 (0.002)	0.00883 (1e10^{-5})
PCA 02010 matrix	15	1176	875 (4)	301	1.37 (0.13)	*n.d.*	3509 (2)	2.849 (0.002)	3508 (3)	2.851 (0.003)	0.00464 (6e10^{-5})

2σ uncertainty in parentheses

n.d.: not determined

Collection of μ-FTIR spectra from thin sections of chondrites has several advantages. First, the *in situ*, spatially resolved spectral measurements can be directly compared to our other spatially resolved measurements of the same section (BSE, EDS, and WDS). We used the correlated datasets to exclude individual spectra that overlapped with areas of fusion crust and terrestrial weathering and to isolate spectral measurements for matrix-only spectra. Second, because all sections are of solid samples, spectral variations due to scattering by small particles (<~65–75 μm) are not an issue. Third, unlike for powdered meteorite samples, which require heating to drive off terrestrial adsorbed water that is introduced during the powdering process (e.g., Beck et al., 2010; Takir et al., 2013; Takir et al., 2019), no sample heating is required. Importantly, this preserves any native, interlayer molecular water that may be present within the phyllosilicate minerals, as well as hydroxyl (OH^-) that is loosely bound due to mineral deformation attributable to impact or regolith gardening on the parent body. Several experiments have shown that phyllosilicate dehydroxylation is enhanced by mechanical deformation and occurs at lower temperatures than heating alone (Drief and Nieto, 1999; Dlugogorski and Balucan, 2014). Therefore, heating chondrite samples may influence the native spectral character of the high-wavenumber region (4000–2500 cm^{-1}; 2.5–4 μm) that probes molecular water and hydroxyl and may affect the tochilinite, sulfates, and Fe-oxyhydroxides within the sample. Finally, we note that the specialized protocol of the NASA Astromaterials Curation Meteorite Thin Section Lab insures that Antarctic meteorite carbonaceous chondrites do not come into contact with water during section preparation and are carefully polished to minimize deformation of the surface (Harrington and Righter, 2017).

Two potential spectral artifacts associated with μ-FTIR spectra on thin sections are interference fringes and spectral contributions from epoxy (Hamilton, 2018). The former is

caused by internal reflections between the parallel surfaces of the section, and are typically most readily observed in areas of high transparency (i.e., low absorption). We removed any individual spectra with strong evidence of fringes. Epoxy is commonly used during the preparation of carbonaceous chondrite thin sections (e.g., Harrington and Righter, 2017). Various types of epoxies are used, but all are variants of thermoplastic resins and have spectral features, mainly associated with hydrocarbons, that are distinct from and much weaker than meteorite mineral spectra in most wavenumber regions (Hamilton, 2018). The only exception is the spectral region near 2900 cm^{-1} (3.4 μm) that contains strong absorptions due to organics in carbonaceous chondrites (e.g., Kaplan et al., 2019). The strong C-H absorptions of the epoxy in this region preclude detailed analysis of native organic spectral features in epoxy-impregnated meteorite thin sections (Supplemental Materials; Fig. SM1).

For each sample map, we identified spectra that contain a substantial amount of epoxy, such as around sample edges and within sample pore space and fractures, in the reflected light image collected by the μ-FTIR instrument (and BSE and EDS maps when available), as well as on the basis of their spectral character, and we deleted these spectra from the map. We averaged the remaining spectra to obtain the average bulk emissivity spectrum of each sample. Some bulk sample spectra still showed evidence of a minor contribution from epoxy in the form of a small, distinctive features around 11150, 1250, and 1500 cm^{-1} (Hamilton, 2018) (Fig. SM1). This is attributed to epoxy that has permeated these relatively porous samples, and we removed it by subtracting a fractional amount of a pure epoxy spectrum from the bulk spectrum using the equation:

$$y = \frac{(y_i - y_e * x)}{(1 - x)} \quad (1)$$

where y is final bulk spectrum, y_i is the initial bulk spectrum, y_e is the pure epoxy spectrum, and x is the fraction of epoxy to remove (values ranging from 0.05 to 0.30), which was determined by visual verification of complete removal of the epoxy feature (Fig. SM1). We calculated the band parameters (described below) of the spectra both with and without the fractional epoxy spectrum removed and found no significant difference in the parameter values. Thus, even though the manual subtraction of epoxy from our bulk sample spectra results in a purer spectral representation of each chondrite sample, this additional data processing step has no influence on the conclusions reached in our study.

For all CMs, we used the BSE and EDS data to select matrix-only μ-FTIR spots within each spectral map. Matrix-only spots were identified based on an absence of chondrules, refractory inclusions, and mineral fragments visibly larger (at the 0.6–0.9 μm/pixel scale of the maps) than the surrounding matrix. We plotted candidate matrix spectra individually to confirm the absence of spectral features of overlooked mineral fragments (olivine, pyroxene, carbonate, or sulfide). We then averaged the matrix spectra (10–33 per sample; Tables 3–4) to obtain the average matrix spectrum for each sample. Similar to the bulk sample spectra, some of the matrix-only spectra exhibited small contributions from epoxy, and these were removed using the fractional epoxy subtraction method described above.

To calculate the band parameters (Tables 3–4) from the averaged bulk sample and matrix-only spectra we first isolated the band and used the POLYFIT function in MATLAB to model it. For all bands, the band minimum [or maximum, in the case of the OH/H_2O band in the high-wavenumber region (4000–2500 cm^{-1}; 2.5–4 μm)] was located by fitting a 6^{th} degree polynomial. For the OH/H_2O band, we also fit a 3^{rd} degree polynomial to the band to determine the band center. We fit seven separate polynomials for all bands by varying (by up to 10 spectral

channels) the bounds of the band. The reported band minimum, maximum, or center is the average of these fits, and the reported uncertainty is 2σ. This is similar to the method of Takir et al. (2013); Takir et al. (2019) for calculating uncertainties on spectral band fits. For the Si-O bending band, the bounds of the band fit were ~490 to ~405cm^{-1}; for the Si-O stretching band, the bounds were ~1050 to ~850 cm^{-1}; for the Mg-OH band, the bounds were ~715 to ~550 cm^{-1}; and for the OH/H_2O band, the bounds were ~3700 to ~3600 cm^{-1} (see Fig. 5 for an example of the polynomial fit to find band center and maximum for the OH/H_2O band).

For all bands except the Si-O bending band, we also calculated band depth. The band depth is defined as the distance between the straight-line continuum bounding the band and the spectral emissivity at the band minimum or maximum. For the Mg-OH band, these local maxima were approximately at ~715 to ~550 cm^{-1}; for the Si-O bending band, ~1050 to 700 cm^{-1}; and for the OH/H_2O band, ~3900 to ~3200 cm^{-1}. For additional characterization of the Si-O stretching band, we calculated two other parameters: the separation between the Christiansen feature (CF; defined as the maximum emissivity between 1300 and 400 cm^{-1}) and the band minimum, and the band symmetry. We define band symmetry as the ratio of the band area (below the straight-line continuum) on each side of the band minimum:

$$\frac{[A(\bar{\nu})]_{\varsigma_2}^{m}}{[A(\bar{\nu})]_{m}^{\varsigma_1}} \quad (2)$$

where A is the area of the band between the designated wavenumbers $\bar{\nu}$ (m is the band minimum, and ς are the continuum points; $\varsigma_2 > \varsigma_1$).

3. Results

3.1 Unheated, aqueously altered CMs

3.1.1 Relative degree of alteration among samples

Because we are investigating the use of IR spectroscopy to distinguish the relative degree of aqueous alteration among CM materials, we also characterized the relative degree of aqueous alteration among our samples using traditional petrographic techniques. We chose two alteration classification schemes, the petrologic subtype of Rubin et al. (2007) and the alteration scale of Howard et al. (2015), because both utilize petrographic and mineralogical data that are available for all of our samples (either through this work or available in previously published studies; Table 1). For five samples, the same sections were previously assigned a petrologic subtype by Friedrich et al. (2018) (Table 1). For ALH 85013, on re-inspection of the section, we reclassified it as a CM 2.2 [cf. CM 2.0 in Friedrich et al. (2018)]. Our section of LEW 90500 differs from that examined by Friedrich et al. (2018), but we confirmed the petrologic subtype of 2.2 assigned by that study. The two Murchison sections are derived from the sample previously examined in detail by Hanna et al. (2015), and we confirmed the petrologic subtype (2.5) assigned by Rubin et al. (2007) for this sample as well.

To determine the alteration scale of Howard et al. (2015) for our samples, we used PSD-XRD data available from previous studies, averaging the data for LAP 02333 from two independent studies (Table 1). We then calculated the phyllosilicate fraction (PSF) and converted this value into the petrographic type as defined by Howard et al. (2015). Although that study refers to this latter value as a "petrographic type", we use the term "alteration index" (Table 1) to discriminate it from the petrologic subtype scale of Rubin et al. (2007). We then use equation 2 of Howard et al. (2015) to convert the alteration index to the equivalent Rubin et al. (2007) petrologic subtype. In this way we can directly compare the relative degree of alteration among the samples that is derived independently using both petrographic observations and bulk

mineralogical data (Fig. 1). Although the bulk mineralogy of CI Alais translates to a PSF of 1.0, we refrain from assigning a petrologic subtype for direct comparison to the CMs, as other observations suggest that the aqueous alteration of most CIs, including Alais, is not complete (as required by PSF 1.0 on the Howard et al. scale) (King et al., 2015).

Although the two scales generally agree on the relative alteration between samples within the small number of CMs studied here (eight), they are only moderately linearly correlated (R^2 = 0.60; Fig. 1). This is a weaker correlation than that found by Howard et al. (2015) (R^2 = 0.88) for the same number of CMs. In addition, we find less distinction in the predicted degree of

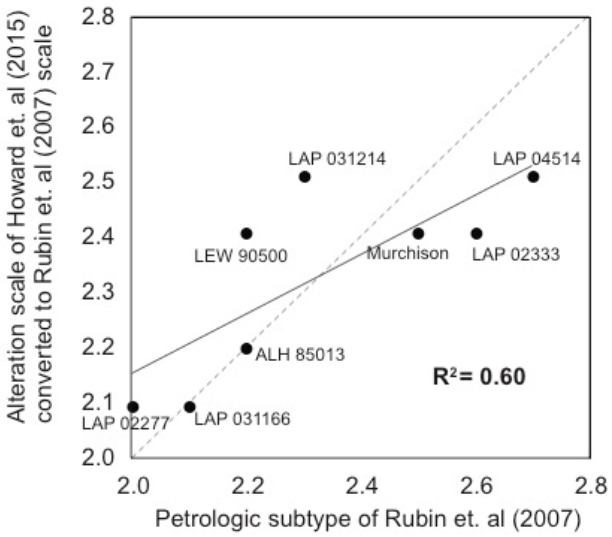

Figure 1. Comparison of CM alteration scales. Petrologic subtype of Rubin et al. (2007) compared to alteration index of Howard et. al (2015) [latter converted to the Rubin et al. (2007) scale using Eq. 2 of Howard et al. (2015)]. The two CM alteration scales are moderately correlated; however, the alteration scale of Howard et. al (2015) appears less sensitive to the relative degree of alteration among the CM suite presented here.

relative alteration among samples using the bulk mineralogy [PSF (Howard et al., 2015)] approach, especially for the less altered CMs, compared to the petrographic observational approach of Rubin et al. (2007). In other words, the Howard et al. (2015) classification scheme appears less sensitive to the relative degree of alteration among the CM suite presented here. Reasons for this discrepancy are explored in Section 4.3, but based on this analysis, we select the relative alteration degree as determined by petrographic observations (i.e., petrographic subtype;

Rubin et al., 2007) as the basis of comparison for the IR spectra of the samples and their derived spectral parameters.

3.1.2 Spectral trends correlated with the degree of aqueous alteration

Infrared spectra of the unheated CMs and CI indicate that several spectral trends are correlated with petrologic subtype (Fig. 2). The CF (~1100 cm^{-1}) shifts to lower wavenumbers and the Si-O stretching band minimum (~950 cm^{-1}) to higher wavenumbers with increasing aqueous alteration. These shifts are linearly correlated (R^2 = 0.82 and 0.65, respectively) with petrologic subtype (Fig. 3A-B). The combination of these shifts also results in a strong

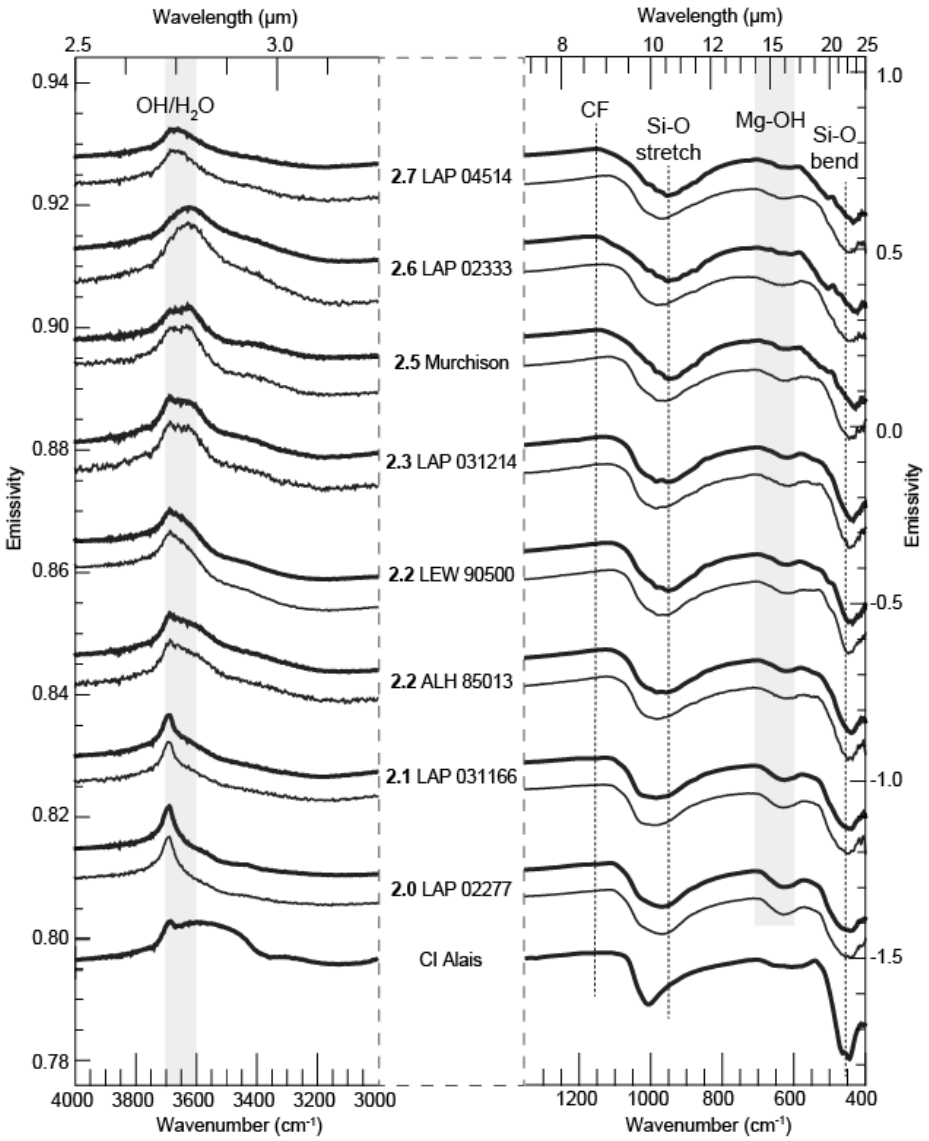

Figure 2. Average bulk sample spectra (thick lines) of eight CMs and 1 CI from least least (top spectrum; LAP 04514, 2.7) to most (bottom spectrum; CI Alais) aqueously altered. Matrix-only spectra (thin lines) of the CMs are also plotted. Spectra are offset (differently for each graph—note the different emissivity scales) and normalized for clarity. Grey boxes and dashed lines highlight spectral features discused in the text.

376

377 correlation (R^2 = 0.90) between the separation distance of the CF and Si-O stretching center and

378 petrologic subtype (Fig. 3C). With increasing alteration, the shape of the Si-O stretching band

379 becomes increasingly assymetric [Eq. (2)] about the band minimum with increasing petrologic

subtype (R^2 = 0.71; Fig 3D), and the bottom of the band becomes more rounded (Fig. 2). CMs with a petrologic subtype of 2.2 or above also have minor bands superimposed on the central part

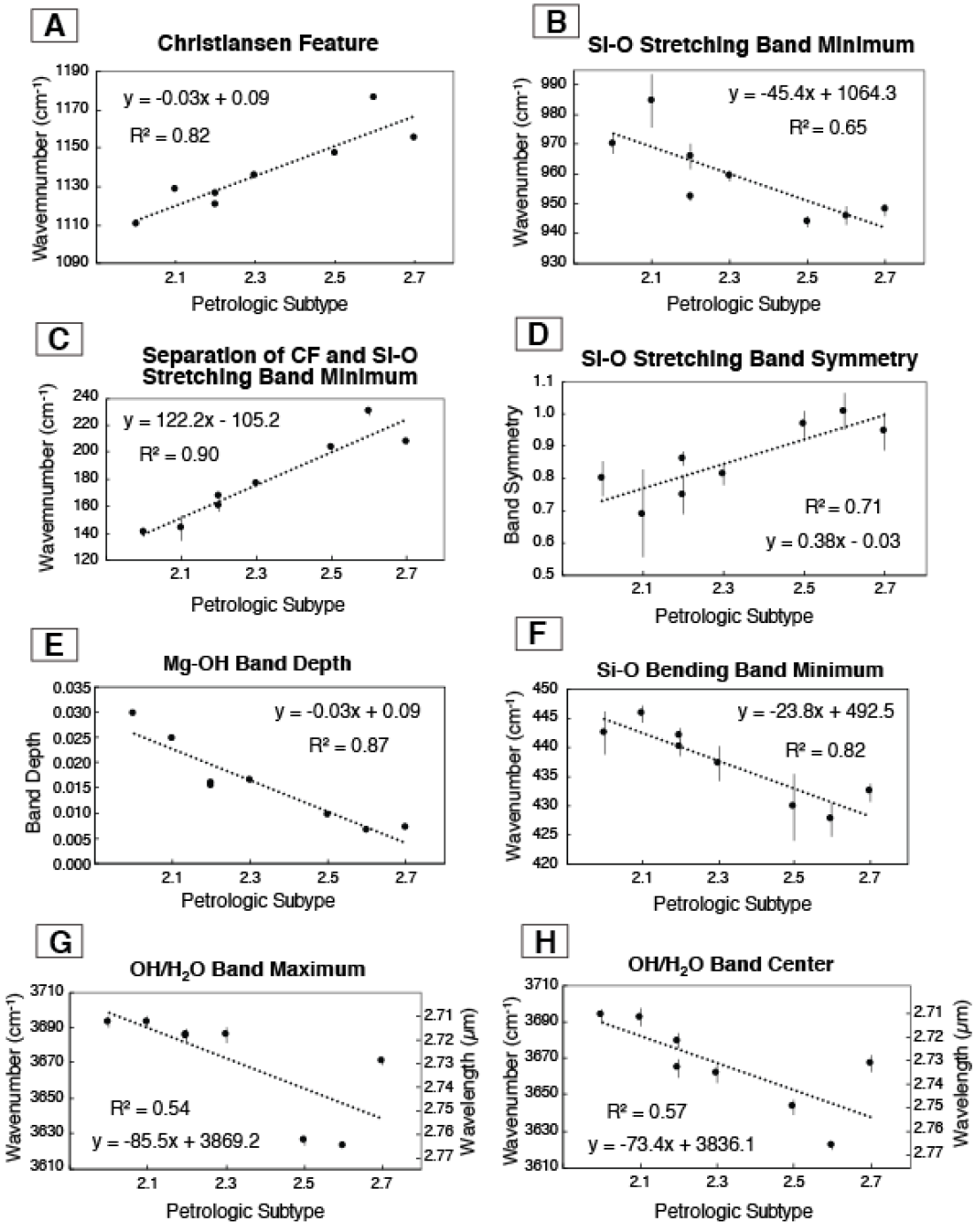

Figure 3. Band parameters of CM spectra in Fig. 2. Vertical bars indicate 2σ.

of the Si-O stretching band that result from the increased abundance of olivine in these samples (Table 1 and Fig. 2). The shallow band centered around 625 cm^{-1} is attributed to a pair of weak absorptions arrising from librations (rotational vibrations) of the inner and surface hydroxyl ions in the octahedral sheet of Mg-bearing serpentine, herein referred to as the Mg-OH band (Farmer, 1974; Michalski et al., 2006). The depth of this band increases as the degree of alteration increases (R^2 = 0.87), although the spectrum of CI Alais does not follow this trend (Figs. 2 and 3E). The lowest wavenumber band has a minimum near 440 cm^{-1} and is a combination of the Si-O bending, Mg-O-Si deformation, and Fe-O-Si deformation bands that overlap in this wavenumber region (Farmer, 1974; Salisbury et al., 1987; Michalski et al., 2006), herein referred to as the Si-O bending band. With increasing petrologic subtype, the Si-O bending band minimum shifts to shorter wavenumbers (R^2 = 0.82; Fig. 3F) and broadens (Fig. 2). A local emissivity maximum also appears on the high wavenumber side of the band near 490 cm^{-1} for the least altered CMs (≥ 2.5; Fig. 2). Both the broadening of the band and this local emissivity maximum are due to the increased abundance of forstertic olivine, which has two major absorptions in this wavelength region (Fig. 4) [see summary by Hamilton (2010) and references therein]. In the most altered CMs (≤ 2.1), a large proportion olivine has been transformed to Mg-Fe phyllosilicate (Table 1), and indeed the CM 2.0 LAP 02277 spectrum shows a strong similarity to an Mg-Fe serpentine spectrum (Fig. 4). Although the CM 2.3 LAP 031214 and CM 2.2 LEW 90500 samples have abundant olivine (Table 1), the olivine maximum near 490 cm^{-1} is subtle.

The other band present in the spectra of all samples, albeit at a greatly reduced spectral contrast compared to the shorter wavenumber bands, is the 3700–3330 cm^{-1} (~2.7–3.0 μm) emission maximum (reflectance minimum) that is associated with OH^- and H_2O (Fig. 2),

406 referred to herein as the OH/H_2O band. The band shape varies among the samples, and in some
407 cases the complexity of the shape means that the band maximum is not aligned with the band
408 center (Fig. 5). Both the band maximum and center vary between 3690 cm^{-1} (~2.71 μm) and

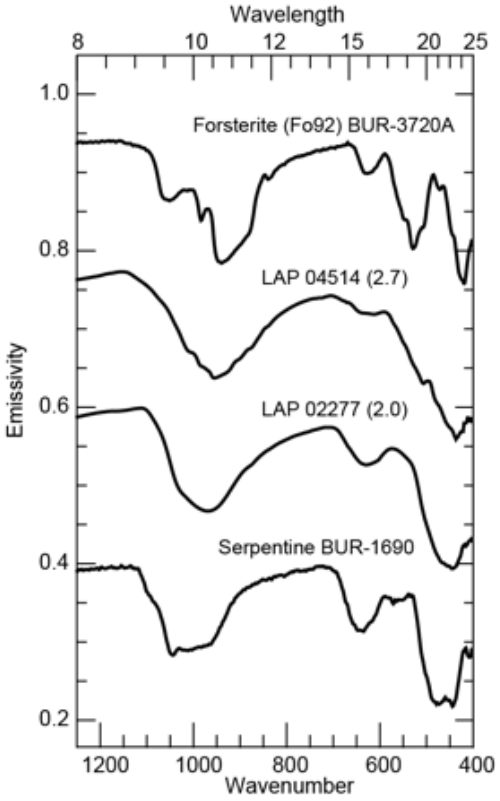

Figure 4. Emissivity spectra of LAP 04514 (CM 2.7) and LAP 02227 (CM 2.0) compared to forsterite (Fo92) and an MgFe serpentine spectra (Christensen et al., 2000). LAP 02277 has a strong similarity in overall spectral shape to the serpentine spectrum, with the same Christiansen feature location and broad, rounded Si-O strecthing, Mg-OH, and Si-O bending bands. The LAP 04514 spectrum has a Christiansen feature location similar to a forsteritic olivine, and a long downward slope from ~17 to ~24 μm that likely results from an increased abundance of olivine, which has two strong absorptions in this wavelength region.

409

410 3623 cm^{-1} (~2.76 μm) and are only weakly correlated (R^2 = 0.54 and 0.57, respectively) with
411 petrologic subtype (Fig. 3G-H). Some of the samples also show increased emissivity on the low
412 wavenumber side (< 3450 cm^{-1}; ≥ 2.9 μm), indicating that molecular H_2O is present (Aines and
413 Rossman, 1984; Salisbury et al., 1987). This is most pronounced in CI Alais but is also
414 discernable in the spectra of ALH 85013, LAP 031214, and LAP 02333. Because these spectra
415 were collected from thin sections and not all sections show evidence of this molecular water, it is
416 probably not the terrestrially adsorbed surface water that contaminates spectra of meteorite
417 powders with much higher surface area (Beck et al., 2010; Takir et al., 2013). Rather, it is likely
418 interlayer or mesopore water, which could be native to the meteorite or of terrestrial origin. To

check for the latter, we examined all unheated CM sections for a spatial correlation between increased emissivity at 3450 cm^{-1} (defined as the difference in emissivity between 3800 and 3450 cm^{-1}) and the edges of the sample, especially when fusion crust was present.

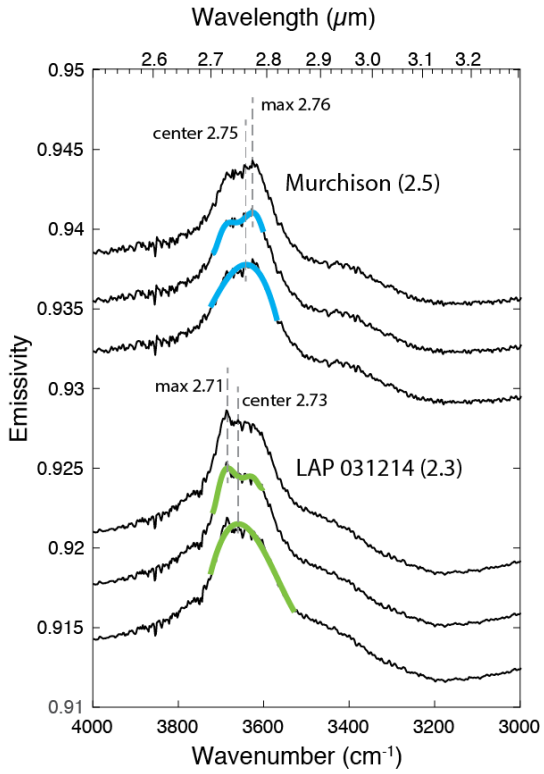

Figure 5. Band center and maximum for two CMs with complex OH/H_2O band shapes that result from a combination of Fe- and Mg-bearing serpentines. The OH/H_2O band of LAP 031214 (2.3) has an emissivity maximum at 2.71 μm indicative of Mg-rich serpentine. The longer wavelength maximum of Murchison (2.5) is consistent with a higher abundance of Fe-bearing serpentine, which has a longer wavelength peak than Mg-rich serpentine.

Both LAP 031166 and LAP 02277 display a clear increased emissivity at 3450 cm^{-1} in areas of fusion crust and nearby regions with dehydration cracks, suggesting that molecular water from terrestrial contamination is present near the sample surface. Because spectra of these areas were excluded from the bulk sample spectra (Section 2.4), this increased emissivity at 3450 cm^{-1} is not present in their bulk sample spectra. The absence of a correlation between increased emissivity at 3450 cm^{-1} and sample edges for the other sections (especially ALH 85013, LAP 031214, and LAP 02333) does not necessarily indicate an absence of terrestrial water contamination, but rather may be the result of the spectral map being located away from the original sample surfaces. None of the sections, however, display any signs of terrestrial

weathering such as carbonate, sulfate, or iron oxide veins (Bland et al., 2006). Most importantly, only CI Alais displays a characteristic molecular water band near 1630 cm^{-1} (Supplemental Materials; Fig. SM2) due to H-O-H bending vibrations (Salisbury et al., 1987; Rossman, 1988), implying that any molecular water within the unheated CM sections is minor and does not substantively affect the shape and position of the OH/H_2O band, especially the position of the band maximum. Finally, we note that most sections display a weak carbonate band near 1500 cm^{-1} that is consistent with its low abundance (≤ 4 %; Tables 1-2) within these samples (Fig. SM2).

Samples of the same petrologic subtype (ALH 85013 and LEW 90500; both 2.2) have very similar CF positions and overall spectral shapes, and their OH/H_2O band maximum and Si-O bending minimum are within uncertainties of each other (Figs. 2 and 3; Table 3). Significant differences between the two samples are in the OH/H_2O band center (lower wavenumber for ALH 85013), Si-O stretching minimum (higher wavenumber for ALH 85013), Si-O stretching symmetry (lower for ALH 85013), and Mg-OH band depth (higher for ALH 85013). The difference in the OH/H_2O band center between the two samples is likely due to the increased emissivity at <3450 cm^{-1} for ALH 85013 that we attribute to the presence of molecular water. The latter three differences all point to ALH 85013 being slightly more altered than LEW 90500, based on the spectral trends among petrologic subtype outlined above and summarized in Figure 3. This is consistent with its higher phyllosilicate abundance and PSF compared to LEW 90500 (Table 1). While the Si-O stretching band minimum and symmetry differences are higher than the average difference between the subtypes, these spectral parameters also have the lowest correlations ($R^2 \leq 0.71$) with subtype. On the other hand, the difference in Mg-OH band depth is much less than the average difference between subtype, which is highly correlated to subtype (R^2

455 = 0.87). In summary, our analysis suggests that the spectral variability among samples of the
456 same petrologic subtype is less than the spectral variability between subtypes, especially in
457 regards to spectral parameters that readily distinguish subtypes (CF, Mg-OH band depth, Si-O
458 bending minimum).
459
460 *3.1.3 Matrix spectra of aqueously altered CM chondrites*
461 Matrix-only spectra are shown in Figure 2 along with their corresponding bulk sample
462 spectra. For individual samples, the averaged matrix spectrum at high wavenumbers (> 3000 cm^{-1})
463 is very similar to that of the bulk sample, with the same general shape and maxima location for
464 the OH/H_2O band, although the matrix-only spectra have a consistently larger OH/H_2O band
465 depth (Table 3), likely attributable to the exclusion of some anhydrous phases that would act to
466 reduce the contrast of this feature. At lower wavenumbers (<1200 cm^{-1}), the bulk sample and
467 matrix spectra are similar for the two most altered CMs (LAP 02277 and LAP 031166) but show
468 increasing differences among less altered CMs (≥ 2.3). First, for the matrix spectra, the CF is at
469 a lower wavenumber and the Si-O stretching band minima are at a higher wavenumber compared
470 to those of the associated bulk sample spectra. The matrix spectra do not show the ~490 cm^{-1}
471 emissivity maximum associated with olivine that is evident in the bulk sample spectra of the less
472 altered CMs, and the ~440 cm^{-1} band of the matrix spectra is also broader with a higher
473 wavenumber mimimum compared to the bulk sample spectra. Thus, the low-wavenumber
474 (<1200 cm^{-1}) matrix spectra do not display the spectral changes correlated with the degree of
475 aqueous alteration that are evident in the bulk sample spectra of these CMs. Rather, the matrix
476 spectra among the differently altered CMs are consistent and generally match the bulk sample
477 spectra of the most altered CMs (≤ 2.1).

Examination of the various band parameters of the matrix-only spectra with respect to petrologic subtype supports these observations. The trend of petrologic subtype with the maximum and center of the OH/H_2O band is essentially unchanged, with correlations of R^2 = 0.54 and R^2 = 0.63, respectively (Supplemental Materials; Fig. SM3). This is expected, as the OH/H_2O band is similar between matrix and bulk sample spectra. For most bands at longer wavelength, linear correlations are low (R^2 < 0.44; ; Fig. SM3), as expected. The only exception is the depth of the Mg-OH band, where there is still a moderate correlation (R^2 = 0.66; ; Fig. SM3), with petrologic subtype among the matrix-only spectra.

3.2 Heated CMs

3.2.1 Petrographic trends associated with degree of heating

Because some aqueously altered samples are known to have undergone subsequent heating (e.g., Nakamura, 2005; Tonui et al., 2014), we also characterized the mineralogical, chemical, textural, and spectral effects of such heating. In addition to the PSD-XRD data presented here, we compiled all available mineralogical and PSD-XRD data for our suite of five heated CMs (Table 2). We use the heating stage scale of Nakamura (2005) to rank the relative heating degree among the samples; in addition, EDS X-ray compositional false-color maps highlight the chemical and textural changes that occur with increased degree of heating (Table 2 and Fig. 6). PSD-XRD data indicates that the abundances of olivine and pyroxene increase and the abundances of amorphous materials and magnetite decrease with increased heating stage (Table 2). Compared to an unheated CM (LEW 90500), Stage II (300–500°C) samples show a more homogenized matrix with an absence of well-defined tochilinite-cronstedtite intergrowths (TCIs; orange-colored phase in LEW 90500 EDS map). The matrices of EET 87522 and EET

96029 are dominated by a dispersed red-colored (in the EDS false color map) phase that is likely composed of Fe-bearing material that has resulted from the breakdown of Fe serpentine (i.e., cronstedtite) and tochilinite, which occurs in Stage II heating (Nakamura, 2005). For WIS 91600, this Fe liberation has resulted in the formation of magnetite and Fe sulfide (Table 2)—which are visible in the map as discrete, bright red phases and diffuse, gold phases, respectively—within the matrix and has been observed by other workers (Brearley, 2004; Tonui et al., 2014). All three Stage II samples have a small proportion of chondrules (< ~10%) with thin dehydration cracks within the fine-grained rims (FGRs) surrounding them. Among these three samples, only WIS 91600 shows obvious mineralogical evidence of terrestrial weathering,

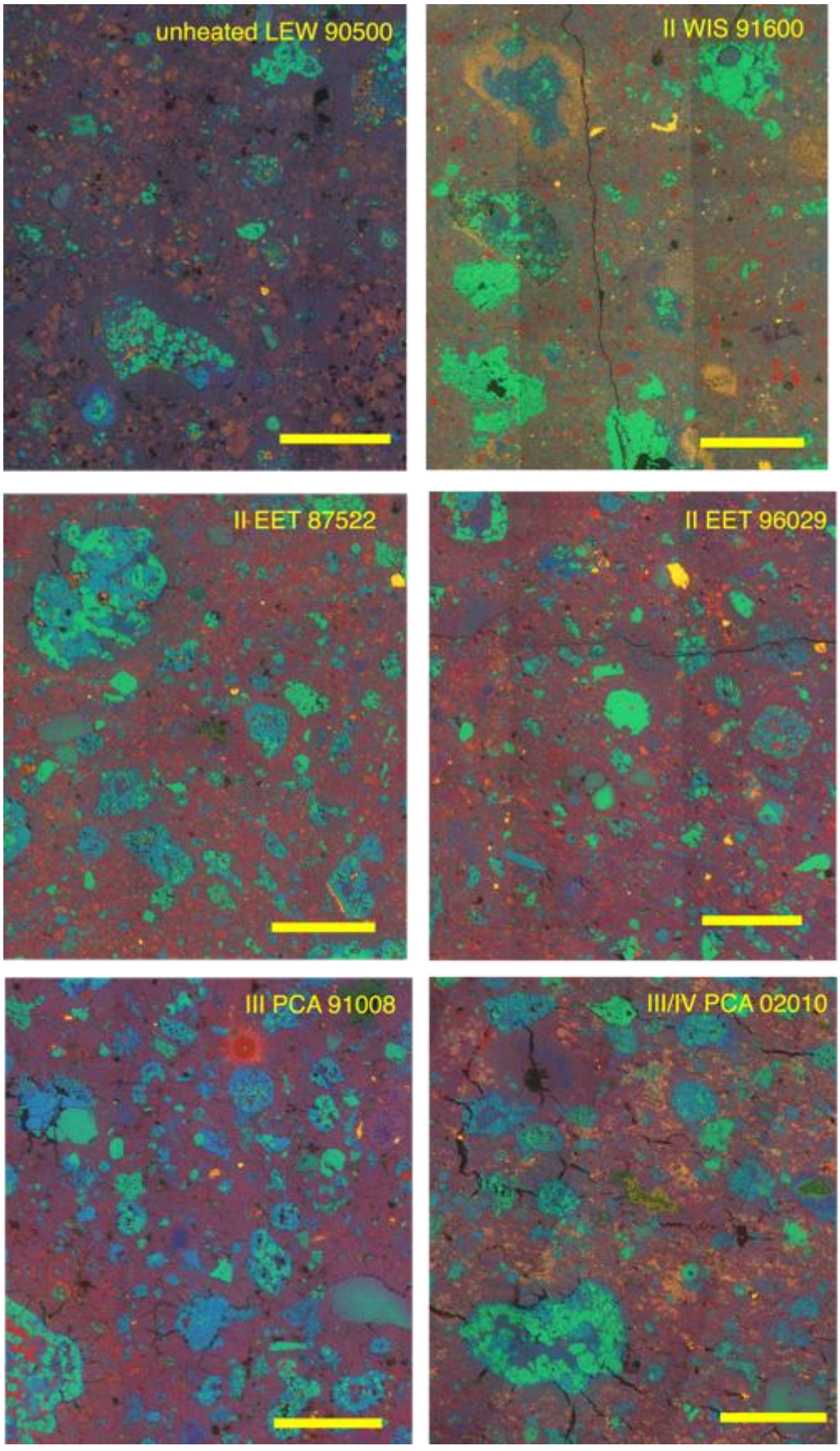
unheated LEW 90500
II WIS 91600
II EET 87522
II EET 96029
III PCA 91008
III/IV PCA 02010

(prev page) Figure 6. EDS X-ray elemental false-color maps highlighting the various phases and textures among the heated CMs. Unheated LEW 90500 is shown for comparison. In all maps, Fe is red, Mg is green, Si is blue, S is yellow, and scale bars are 500 μm. The brightest green and blue phases within the chondrules in all maps are Mg-olivine and Mg-pyroxene, respectively. Fe sulfide and tochilinite are yellow to orange, and pure red phases are primarily magnetite with minor metal.

510

511 with a diffuse Mg-bearing, Si- and Fe-poor phase distributed in an elongated patch that is parallel
512 to the fusion crust. Isolated spectra of this phase show a band near 1600 cm^{-1} (Supplemental
513 Material; Fig. SM2) due to H-O-H bending vibrations (Aines and Rossman, 1984; Salisbury et
514 al., 1987), so we tentatively interpret this phase as a Mg-bearing, terrestrial hydrated evaporite
515 such as hydromagnesite (Bland et al., 2006).

516 The more highly heated [> 500°C; (Nakamura, 2005)] CMs PCA 91008 and PCA 02010
517 display more pronounced textural changes, although the abundant secondary olivine that has
518 crystallized within their matrices (Table 2) is not visible at the scale of the EDS maps (Fig. 6).
519 The matrix of Stage III (500 – 750°C) PCA 91008 is even more chemically and texturally
520 homogenized than that of the Stage II CMs, and dehydration cracks within FGRs are more
521 abundant (Fig. 6). A large magnetite nodule is evident at the top of the map and within the
522 chondrule at the lower left, which is consistent with the moderate abundance (2.7 vol. %) of
523 magnetite in this sample (Table 2). The X-ray map shows signs of Fe diffusion from the large
524 magnetite nodule into the surrounding matrix, likely caused by terrestrial alteration ['rusts' were
525 detected via PSD-XRD in another aliquot of this sample; Table 2)]. The most extensively heated
526 CM, Stage III/IV (>750°C) PCA 02010, has abundant large dehydration cracks around
527 chondrules and within the matrix, and, similar to WIS 91600, diffuse patches of Fe-sulfide are
528 visible within the matrix (Table 2 and Fig. 6). The chondrules in PCA 02010 also appear
529 'blurred', a texture that has been previously noted in highly heated CMs, suggesting incipient
530 recrystallization and integration with the surrounding matrix (Tonui et al., 2014). Also visible in

the upper left corner is a thin crack filled with Fe oxide (rust) from terrestrial weathering; similar cracks are seen elsewhere in this section and range in width from 8 to 20 μm. The detection of feldspar (3.2%; Table 2) with PSD-XRD indicates that PCA 02010 may be a stage IV or even higher, as feldspar is found within PCA 02012 [estimated to have been heated to 900°C (Nakato et al., 2013)] and is also present in thermally metamorphosed type 3 chondrites (Grossman and Brearley, 2010).

3.2.2 *Spectral trends associated with degree of heating*

The bulk sample IR spectra among the heated CMs show differences associated with their relative heating stage (Fig. 7). Several band parameters also show a general correlation with degree of heating (Table 4), although we did not test for a linear correlation due to the small sample size, especially in regards to the heating stages represented. The CF shifts to slightly higher wavenumbers and the Si-O stretching band minimum to lower wavenumbers for the Stage III–III/IV than for the Stage II CMs. This translates to an increase in the separation distance between the CF and Si-O stretching band minimum as heating proceeds (Table 4). The Stage III–III/IV CMs also have a generally more symmetric Si-O stretching band shape than the weakly heated samples. This is unsurprising as the Stage III and III/IV samples show a markedly different band shape that is sharper with several overlapping bands not present in the Stage II samples. These overlapping bands are most evident in PCA 02010 as two small shoulder bands at 965 and 833 cm^{-1} on either side of the Si-O stretching minimum that are consistent with the olivine that dominates this sample (Hamilton, 2010; Beck et al., 2014), some of which is secondary (Table 2). These olivine shoulder bands are weaker in the PCA 91008 spectrum, consistent with this sample's lower olivine abundance (Table 2). The positions of

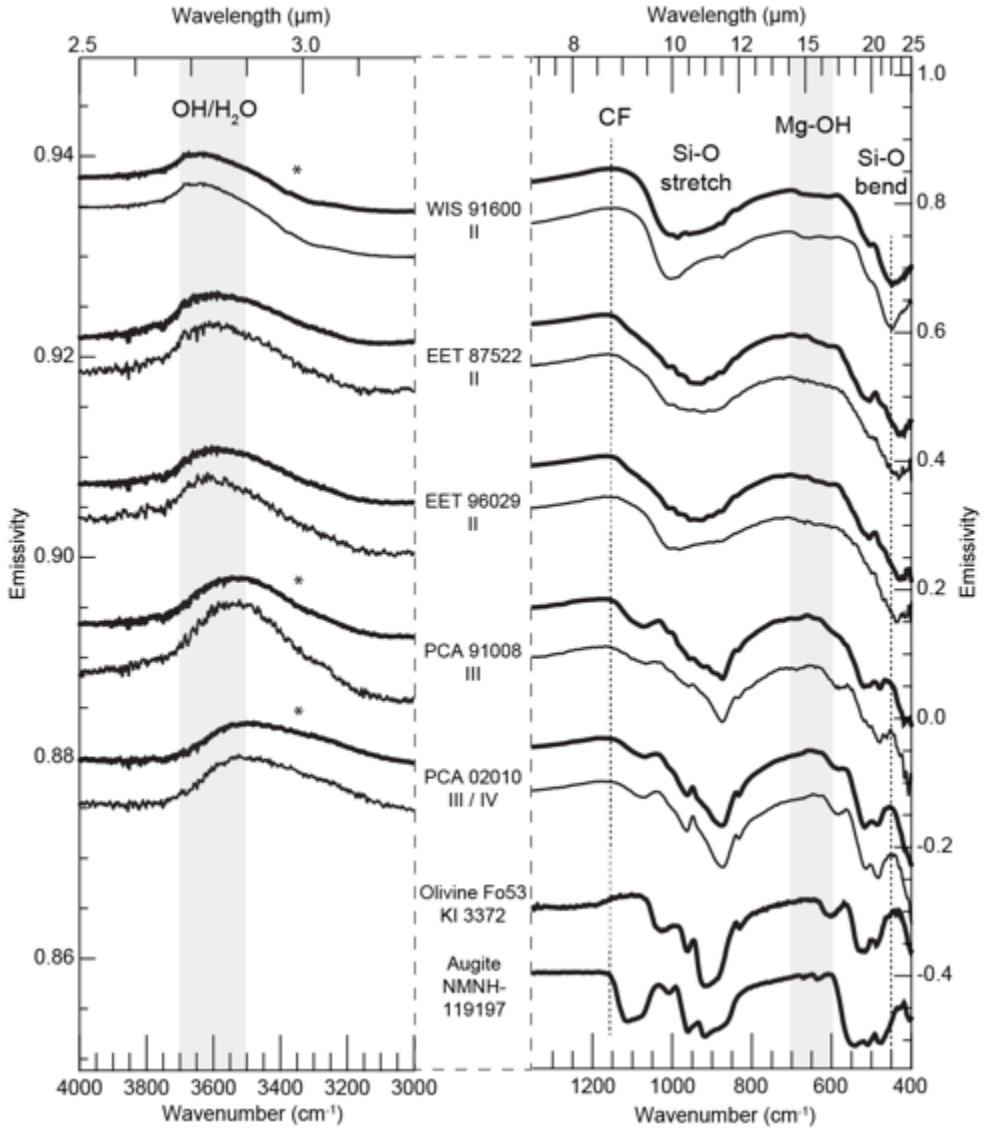

Figure 7. Average bulk sample (thick line) and matrix (thin line) spectra of five thermally metamorphosed CMs from least (top spectrum) to most (bottom spectrum) heated according to the heating stage of Nakamura (2005). The olivine Fo53 spectrum is from Koeppen and Hamilton (2008) and Hamilton (2010), and the augite spectrum is from Hamilton (2000) and Christensen et al. (2000). Asterisks denote evidence that the 3-μm band has been contaminiated by terrestrial weathering. Spectra are offset (differently for each graph—note the different emissivity scales) and normalized for clarity. Grey boxes and dashed lines highlight spectral features discused in the text.

these shoulder bands vary with the Mg content (Fo#) of the olivine and here are most consistent with an olivine of intermediate (Fo_{50-70}) composition (Koeppen and Hamilton, 2008; Hamilton, 2010) (Fig. 7). All heated samples except WIS 91600 show numerous minor bands superimposed throughout the Si-O stretching region that are characteristic of Mg-rich, high-Ca

559 pyroxene (Hamilton, 2000) and olivine (Duke and Stephens, 1964; Burns and Huggins, 1972;
560 Hamilton, 2010) consistent with the PSD-XRD results (Fig. 7, Table 2). A band at ~1085 cm^{-1},
561 also indicative of pyroxene (Hamilton, 2000), is present in the samples heated to Stage III and
562 above (Fig. 7). While EET 96029 also has a relatively high pyroxene abundance (15.7%; Table
563 2), this band is masked by the Si-O stretching band of the amorphous silicate (64.7%; Table 2).
564 At lower wavenumbers (<600 cm^{-1}), the bulk sample spectra for all heated CMs show
565 features generally attributable to the presence of olivine and pyroxene (Fig. 7) in differing
566 proportions. All Stage II samples have a broad Si-O bending band with a local emissivity
567 maximum near 490 cm^{-1} that is present in the least aqueously altered CMs (Fig. 2). Because
568 these samples have not yet formed secondary olivine (Table 2) due to their low heating stage
569 (Nakamura, 2005), this spectral feature represents primary olivine in the samples. The more
570 highly heated samples PCA 91008 and PCA 02010 both show spectral features associated with
571 Fe-bearing olivine and pyroxene in this region, with absorptions near 588, 518, and 479 cm^{-1}
572 (Duke and Stephens, 1964; Hamilton, 2000; Hamilton, 2010). These bands are more pronounced
573 in the more extensively heated PCA 02010 despite the similar olivine and pyroxene abundances
574 in these two samples (Table 2), likely indicating that these phases are more crystalline than in
575 PCA 91008, which is consistent with its higher heating stage (Nakamura, 2005). Additionally,
576 although difficult to verify because it is at the edge of our spectral range, it appears that the band
577 minimum of the Si-O bending band moves to lower wavenumbers with increasing thermal
578 metamorphism and is less than 400 cm^{-1} for PCA 91008 and PCA 02010—also consistent with
579 an Fe-bearing olivine (Hamilton, 2010).
580 The 3700–3300 cm^{-1} (2.7–3.0 μm) OH/H_2O band emission maximum consistently moves
581 to lower wavenumbers with increased degree of heating, from 3643 cm^{-1} (2.75 μm) to 3495 cm^{-1}

582 (2.86 μm) (Table 4 and Fig. 7). In all samples, this band is broad, with a band center that
583 overlaps its band maximum within their uncertainties (Table 4), and a broad shoulder is present
584 with increased emissivity on the low wavenumber side (< 3450 cm^{-1}; ≥ 2.9 μm), suggesting that
585 molecular H_2O is present (Aines and Rossman, 1984; Salisbury et al., 1987). Like for the
586 unheated CM sections, we checked for an increased emissivity at 3450 cm^{-1} near sample
587 surfaces, and only PCA 91008 showed a slight increase near the fusion cust. No fusion crust is
588 visible in the sections of EET 87522, EET 96029, and PCA 02010, and for WIS 91600 there is
589 no increase in 3450 cm^{-1} emissivity with proximity to its fusion crust. Previous studies have
590 noted that the OH/H_2O bands of PCA 91008 and PCA 02010 are deeper than expected and
591 therefore have been affected by terrestrial weathering (Tonui et al., 2014; King et al., 2016). Our
592 data supports this interpretation as both samples show mineralogical evidence of terrestrial
593 weathering (Section 3.2.1) and display prominent OH/H_2O bands despite their IR spectra at
594 lower wavenumbers (<1200 cm^{-1}) being dominated by olivine and pyroxene spectral features
595 (Fig. 7). There is also no PSD-XRD evidence for hydrous phases within these samples (Table
596 2). Because WIS 91600 displays a band near 1600 cm^{-1} that could be attributed to molecular
597 water (Aines and Rossman, 1984; Salisbury et al., 1987) (Supplemental Materials; Fig. SM2),
598 and there is considerable terrestrial weathering in this section (Section 3.2.1), its OH/H_2O band
599 likely has also been affected by terrestrial weathering.
600
601 3.2.3 *Matrix spectra of heated CM chondrites*
602 At wavenumbers lower than 1200 cm^{-1}, the matrix-only spectra differ from the bulk
603 sample spectra of the heated samples (Fig. 7). The matrix-only spectra of WIS 91600 and EET
604 96029 both exhibit a more asymmetric shape and higher wavenumber minimum for the Si-O

605 stretching band relative to their bulk sample spectra (Fig. 7 and Table 4). The matrix spectrum
606 of PCA 91008 shows a narrower Si-O stretching band with a weaker pyroxene band near 1085
607 cm^{-1} compared to its bulk spectrum. The Si-O stretching band of PCA 02010 is similar in the
608 matrix and bulk sample spectra, although the olivine and pyroxene bands may be slightly deeper
609 in the matrix spectrum. All three Stage II CMs have a noticeably weaker or absent emissivity
610 maximum near 490 cm^{-1} (attributable to olivine) in their matrix-only spectra. For the more
611 highly heated CMs PCA 91008 and PCA 02010, the largest differences between the matrix and
612 bulk sample spectra are in the strength of the olivine bands near 588 and 479 cm^{-1}, which are
613 both stronger in the matrix-only spectra. For PCA 91008, the 588 cm^{-1} olivine band is not
614 discernable in the bulk sample spectrum.

615 The 3700–3330 cm^{-1} (2.7–3.0 μm) OH/H_2O band emission maximum of the matrix-only
616 spectral shape is very similar to that of the bulk sample spectrum of the heated CMs, although
617 the band maximum of the matrix is at a slightly higher wavenumber (by 6–26 cm^{-1}) for all
618 samples except EET 87522 (Table 4). Another difference between matrix and bulk sample
619 spectra in this wavelength region is that the OH/H_2O band depth of the matrix-only spectrum is
620 consistently greater than for the bulk sample spectrum (Table 4), as was found for the unheated
621 CMs, and probably represents the exclusion of some fraction of anhydrous phases.
622

623 ## 4. **Discussion**

624 ### *4.1 Low-wavenumber (<1200 cm^{-1}) spectral indicators of secondary processes in CMs*

625 #### *4.1.1 Aqueous alteration indicators*

626 There are several spectral trends in the IR at wavenumbers <1200 cm^{-1} that can be correlated
627 with the relative degree of aqueous alteration among the CMs. At this wavenumber range,
628 spectral features are dominated by both hydrated and anhydrous silicates. With increasing

degree of aqueous alteration (i.e., lower petrographic subtype), the CF moves to lower wavenumbers, the Si-O stretching (~950 cm^{-1}) and Si-O bending (~440 cm^{-1}) band minima move to higher wavenumbers, the separation of the CF and Si-O stretching band minimum decreases, and the depth of the Mg-OH band (~625 cm^{-1}) increases (Figs. 2-3). The strongest correlation with petrographic subtype (R^2 = 0.90) is the separation of the CF and Si-O stretching band minimum, and using the equation defined by the linear fit of that relationship:

$$petrologic\ subtype = \frac{y+105.2}{122.2} \quad (3)$$

the petrologic subtype of the sample is predicted to within 0.1 accuracy based on the measurement of the separation *y* in wavenumbers for the sample suite presented here.

Because all CMs are volumetrically dominated by phyllosilicates, and their proportion increases with aqueous alteration (Table 1; see also Howard et al., 2015), the CF and spectral bands are dominated by hydrous silicates, with contributions from the anhydrous silicates olivine and pyroxene in the least altered CMs (Fig. 4), as noted by previous workers (Sandford, 1984; Beck et al., 2014; Beck et al., 2018). Therefore, the shifting of these bands (and change in depth for the Mg-OH band) could reflect the relative abundance, structure, and composition of the phyllosilicate that shifts from an Fe-bearing serpentine (i.e., cronstedtite) to a more Mg-dominated serpentine as alteration proceeds (Tomeoka et al., 1989; Zolensky et al., 1993; Browning et al., 1996). The depth of the Mg-OH band, which is attributable to Mg-bearing serpentine, is consistent with this interpretation, as it systematically increases with decreasing petrologic subtype (R^2 = 0.87) (Figs. 2 and 3E). Olivine, which has higher abundances within the least altered CMs (Table 1), also has an absorption in this region (narrower and centered at a slightly lower wavenumber) but has a relatively weaker spectral signature compared to Mg-bearing serpentine (Fig. 4). However, the other spectral parameters (CF, Si-O stretching

minimum, Si-O stretching symmetry, and Si-O bending minimum) are significantly influenced by the presence of olivine, as well as pyroxene, which have strong aborptions in these regions (Figs. 4 and 7). In the Si-O stretching region, the presence of these anhydrous silicates in the least altered CMs causes a strong absorption at a lower wavenumber than serpentine, which results in a movement of the Si-O stretching minimum to a lower wavenumber, as well as a more symmetrical band shape (Fig. 2). The CF likewise shifts to higher wavenumbers with increasing anhydrous abundance due to the higher wavenumber CF of olivine and pyroxene compared to serpentine. In the Si-O bending region, as the proportion of serpentine increases with alteration, this band is less influenced by the strongest olivine absorption near 420 cm^{-1}, and the band minimum shifts to higher wavenumbers (Fig. 2). In summary, the spectral trends at wavenumbers <1200 cm^{-1} among the unheated, aqueously altered CMs are a result of the mineralogical and compositional changes as ferromagnesian silicates are altered to increasingly Mg-rich phyllosilicates (Zolensky et al., 1997; Rubin et al., 2007; Howard et al., 2015). Specifically, as olivine and pyroxene are replaced by phyllosilicate with increasing degree of alteration among the CMs (Rubin et al., 2007; Howard et al., 2015), all bands become relatively more influenced by the phyllosilicate (serpentine) compared to the anhydrous silicates (primarily olivine but also pyroxene).

4.1.2 Thermal metamorphism indicators

With subsequent heating of the CMs, several spectral features at low wavenumber (< 1200 cm^{-1}) are associated with the different heating stages. First, the Si-O stretching band broadens (Stage II) and then, with higher heating stages (Stage III+), becomes sharp with noticeable olivine bands with positions consistent with Fe-bearing olivine (Fig. 7) that can be attributed to

676 secondary olivine formation (Nakamura, 2005). The Si-O bending minimum also shifts to lower
677 wavenumbers with heating, forming strong olivine bands in the 500 cm^{-1} region. We attribute
678 the initial broadening of the Si-O stretching band in the mildly heated (Stage II) samples to the
679 thermal decomposition of phyllosilicates, which several studies have shown forms a highly
680 disordered, amorphous phase that is intermediate to the secondary olivine formed at higher
681 temperatures (Akai, 1988; Nakamura, 2005; Tonui et al., 2014). Amorphous and poorly
682 crystalline phases typically result in broader Reststrahlen bands relative to their well-crystalline
683 counterparts due to the wide range of site sizes and symmetries and variable orientations of
684 molecules within those sites (Farmer, 1958; Gaffey et al., 1993b). Although the spectral changes
685 for CMs heated at ≥ Stage III are readily visible as strong bands from the secondary olivine
686 appear, the changes associated with only mild heating (Stage II) are subtle. Further, because the
687 original petrologic subtype (i.e., 2.0 to 2.7) of the Stage II samples is not known, some of these
688 spectral modifications may not be attributable to mild heating and thus are ambiguous.
689 Some of this ambiguity may be resolved with other observations, however. First, if we
690 assume that the amorphous component for the Stage II samples was originally phyllosilicate, we
691 can calculate the PSF prior to thermal metamorphism to derive an alteration index. For EET
692 96029, this results in an alteration index of 1.6 [petrologic subtype 2.5 (Howard et al., 2015)]; for
693 EET 87522, 1.5 (petrologic subtype 2.4); and for WIS 91600, 1.3 (2.2). For the mildly heated
694 EET 96029, Lee et al. (2016) assigned a pre-heating petrologic subtype of 2.7 based on detailed
695 observations of components least likely to be affected by mild heating, including chondrule
696 mesostasis and Fe,Ni metal. Because the low stage of heating (II) for EET 96029 precludes the
697 formation of secondary olivine, the emissivity maximum near 490 cm^{-1}, attributable to olivine,
698 must represent primary olivine, similar to the least aqueously altered CMs (≥ 2.5; Fig. 2). This

699 olivine signature is very weak in the matrix-only spectrum of EET 96029 (Fig. 7), suggesting
700 that, as for the unheated CMs, the olivine is primarily located within the chondrules and other
701 large inclusions (i.e., not the fine-grained matrix). The isolation of the olivine spectral signature
702 to the chondrules [as opposed to the matrix, where heating effects and secondary products are
703 concentrated (Nakamura, 2005)], further supports that EET 96029, despite mild heating, can be
704 classified as a very mildly aqueously altered CM, as suggested by Lee et al. (2016). The 490
705 cm^{-1} olivine feature is also present in the spectra of WIS 91600 and EET 87522, suggesting that
706 they were also only mildly aqueously altered prior to heating, although the relatively smaller 490
707 cm^{-1} emissivity minimum, the lower wavenumber position of its CF, and absence of the minor
708 pyroxene bands in its Si-O stretching region suggests that WIS 91600 has experienced more
709 aqueous alteration than EET 87522 and EET 96029. This is supported by the estimation of its
710 alteration index prior to heating (1.3), which is lower than for EET 87522 (1.5) and EET 96029
711 (1.6).

712 Because we have established, both from the prior petrographic work of Lee et al. (2016)
713 and the spectral data presented here, that EET 96029 is a relatively unaltered CM (2.7), we can
714 now further confirm the specific spectral changes that occur solely from mild heating by
715 comparing the spectrum of EET 96029 to that of another CM 2.7 (LAP 04514) that has not been
716 heated (Fig. 8). Between these samples, the spectral band with the largest amount of

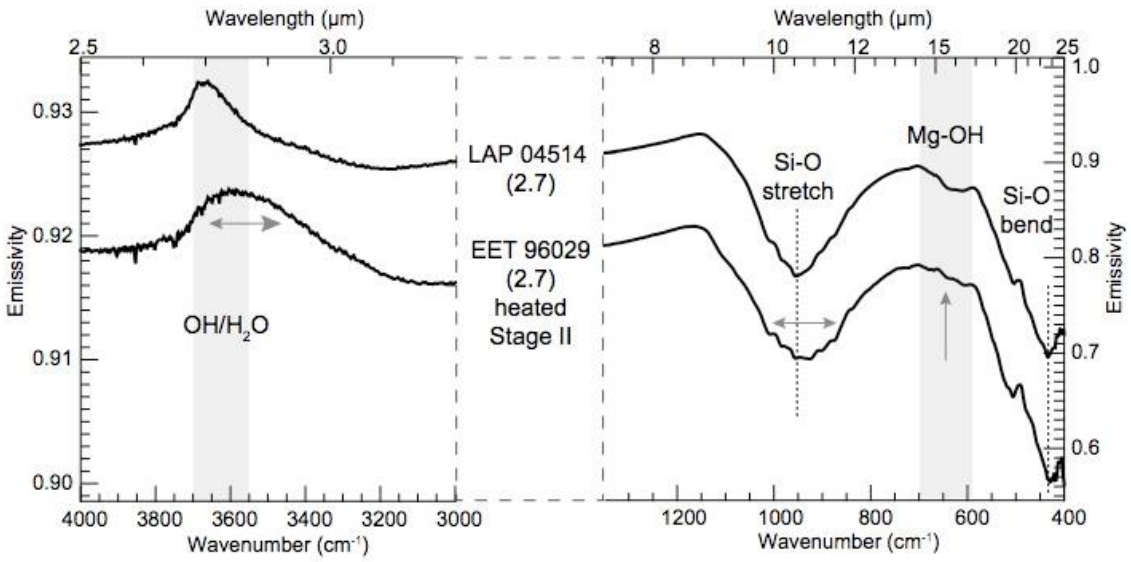

Figure 8. Unheated LAP 04514 (2.7) compared to mildly heated Stage II EET 96029 (2.7). Grey arrows and boxes highlight the spectral changes associated with mild heating. With mild heating, the Si-O stretching band broadens (right horizonal arrow) and its minimum shifts to smaller wavenumber (left dashed line), the Mg-OH band disappears (vertical arrow and grey box) and the OH/H_2O band broadens and moves to longer wavelengths (left horizontal arrow and grey box), although this may also be due to rehydration from terrestrial weathering (see Section 4.2). There is no significant change in the location of the Si-O bending minimum (right dashed line). Spectra are offset (differently for each graph—note the different emissivity scales) and normalized for clarity.

717

718 modification with heating is the Si-O stretching region. First, the CF location is different
719 between them (1165 cm^{-1} for EET 96029 and 1155 cm^{-1} for LAP 04514). This difference could
720 be the result of heating; however, the position of the CF is highly sensitive (i.e., highly
721 correlated; $R^2 = 0.82$) to the degree of aqueous alteration due to the varying proportions of
722 phyllosilicate and anhydrous silicates as discussed above. In addition, when examining samples
723 of the same petrologic subtype (ALH 85013 and LEW 90500; both 2.2), the CF location differs
724 by 13 cm^{-1} (greater than the 10 cm^{-1} here). Therefore, although mild heating could cause the CF
725 to shift to a higher wavenumber, as it does for strongly heated samples (Table 4; Fig. 7), it is
726 more difficult to attribute this solely to heating rather than to a minor difference in degree of
727 aqueous alteration, even within the same petrologic subtype. The other major change within the

728 Si-O stretching region is that for the mildly heated EET 96029, the band is wider and less sharp
729 at the minimum than that of LAP 04514, and its band minimum is at lower wavenumber (935 ± 4
730 cm^{-1}) than for LAP 04514 (946 ± 2 cm^{-1}). The other band that is modified by mild heating is the
731 Mg-OH band, which is present, although weak, in the LAP 04514 spectrum, but absent from the
732 EET 96029 spectrum. Finally, the Si-O bending minima for LAP 04514 and EET 96029 are
733 within the 2σ uncertainty of one another (432 and 428 cm^{-1}), indicating that no significant shift
734 of this band occurs with mild heating.

735 In summary, within the low-wavenumber region (<1200 cm^{-1}), where spectral features
736 are dominated by both hydrated and anhydrous silicates, the largest effect of mild heating is a
737 broadening of the Si-O stretching band, a low-wavenumber shift of its band minimum, and the
738 disappearance of the Mg-OH band (Fig. 8). The broadening and shifting of the Si-O stretching
739 band are also seen in experimental space weathering studies of simulated solar wind irradiation
740 in CMs (Lantz et al., 2015; Lantz et al., 2017; Brunetto et al., 2018), which is unsurprising as ion
741 irradiation results in the amorphization of silicates (Brucato et al., 2004; Demyk et al., 2004).
742 However, it appears that simulated space weathering of this type does not noticeably affect the
743 depth of the Mg-OH band (Lantz et al., 2017), which could help distinguish the effects of mild
744 heating from space weathering on an asteroidal surface. More work is needed in this area.
745
746 *4.2 Modification of the OH/H_2O band with aqueous alteration and heating*

747 The OH/H_2O band is also modified as the degree of aqueous alteration or heating changes
748 among our CM suite. However, the correlation of band center or band maximum with petrologic
749 subtype is weak (Fig. 3G-H), and some of the heated CMs may be affected by terrestrial
750 weathering (Section 3.2.2; Fig. 7). Among the unheated CMs, the OH/H_2O band maximum for

751 subtypes 2.0–2.3 are all located at 2.71 μm (Table 3). This 2.71-μm maximum of the highly
752 altered CMs coincides with the band maximum of Mg-rich serpentines lizardite and chrysotile
753 (Calvin and King, 1997; Post and Borer, 2000; Takir et al., 2013). The three higher petrologic
754 subtypes (≥ 2.5) have maxima at longer wavelengths, although the maximum for LAP 04514
755 (2.7) is only at 2.72 μm, whereas Murchison (2.5) and LAP 02333 (2.6) are both located at 2.76
756 μm. This shift of the OH/H_2O band maximum to longer wavelengths is consistent with a
757 contribution from Fe-bearing serpentines that display an OH^- peak longward of ~2.74 μm
758 (Calvin and King, 1997; Cloutis et al., 2008; Takir et al., 2013; Bates et al., 2020). Similar to the
759 findings of previous studies, the spectral shape of this band in our CMs does not exactly match
760 any terrestrial Fe-bearing serpentine collected to date (Calvin and King, 1997; Takir et al., 2013).
761 We hypothesize that the presence of Fe-bearing serpentine in the least altered CMs is causing a
762 wider, more complex OH/H_2O band that is a combination of both Mg- and Fe-serpentine (Figs. 2
763 and 5); a similar conclusion was reached by Beck et al. (2010). In LAP 031214 (2.3), the Mg-
764 serpentine is more dominant, causing a peak at 2.71 μm, but in Murchison (2.5), the Fe-
765 serpentine peak at 2.76 μm is higher, suggesting more Fe-bearing serpentine relative to Mg-rich
766 serpentine (Fig. 5). This interpretation is consistent with their relative petrologic subtypes,
767 where the dominant phyllosilicate phase becomes Mg-rich serpentine with increasing aqueous
768 alteration (decreasing petrologic subtype) (Tomeoka et al., 1989; Zolensky et al., 1993;
769 Browning et al., 1996; Rubin et al., 2007), and with their ratios of measured Mg-rich serpentine
770 to Fe-rich serpentine (1.3 for LAP 031214 and 0.44 for Murchison; Table 1). This is also
771 consistent with Calvin and King (1997), who found that the shape of OH/H_2O band in Murchison
772 was best approximated with a linear combination of both Mg- and Fe-bearing phyllosilicates.

773 Another hydrated phase that may be contributing to the shape and location of the
774 OH/H_2O band is tochilinite, which has an absorption band in this region (Moroz et al., 2006) and
775 is commonly intergrown within Fe-serpentine (cronstedtite) in the less altered CMs (Mackinnon
776 and Zolensky, 1984; Tomeoka and Buseck, 1985; Zolensky et al., 1993; Lauretta et al., 2000).
777 Unfortunately, there is no pure tochilinite standard that allows reliable determination of its
778 volume abundance in CMs using PSD-XRD (Howard et al., 2011), but estimates based on mass
779 balance calculations and modal analysis from point counting are up to 8 vol.% and likely higher
780 for the least altered CMs (Zolensky et al., 1993; Howard et al., 2011). Moroz et al. (2006)
781 measured the reflectance minimum (emissivity maximum) of synthetic tochilinite at 2.78 μm,
782 which is a shorter wavelength minimum than for cronstedtite (~2.85 μm), although the latter
783 could be influenced by adsorbed water (e.g., Takir et al., 2013). We identified a large (~200 μm)
784 clump of tochilinite in the section of LAP 02333 (2.6) with significant Fe, S, Cr, Ni, and P,
785 moderate O, and negligible Mg and Si (determined via EDS Kα peak mapping); we collected an
786 isolated μ-FTIR spectrum (Fig. 9). Our tochilinite spectrum shows an emission peak near 2.79

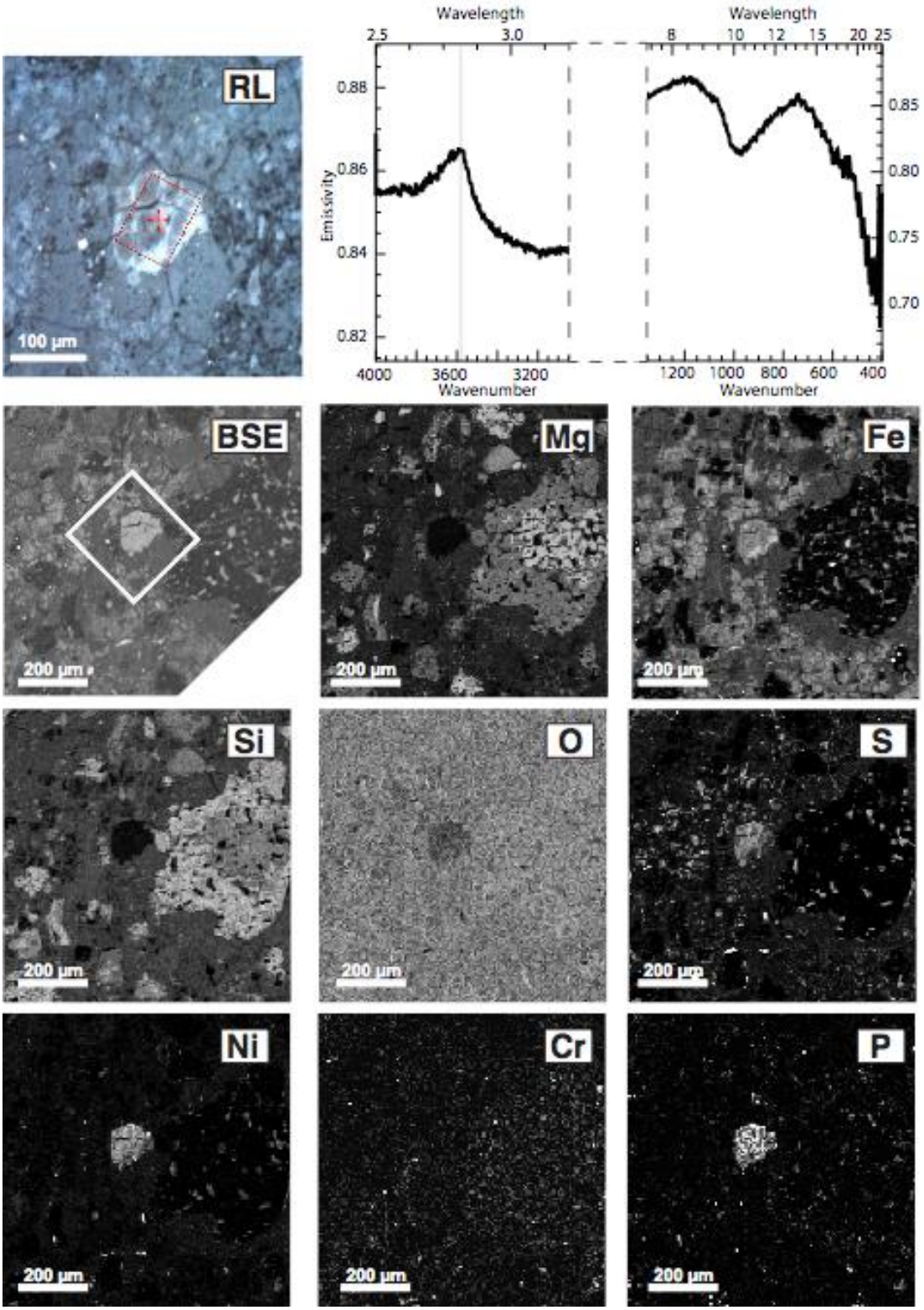

Figure 9. Tochilinite inclusion in CM 2.6 LAP 02333. RL: Reflected light image showing location (box) of IR spectrum to right (note different emissivity scales for the two sides of the plot to the right). Grey line marks the emissivity maximum of the OH band at 3585 cm^{-1} (2.79 µm). BSE: BSE image

highlighting tochilinite inclusion (white box). The other images are EDS maps of the *[Fig. 9 caption continued from previous page]* designated element. Neglible Mg and Si with high Fe, S, and Ni, and the absence of a 2.71 µm Mg-OH spectral band, confirms that the inclusion is nearly pure Fe-rich tochilinite.

787

788 µm but—unlike the synthetic tochilinite measured by Moroz et al. (2006)—tochilinite in LAP
789 02333 does not show the sharp Mg-OH peak at 2.71 µm. The absence of this peak confirms that
790 significant Mg is not present in this meteoritical tochilinite. Our tochilinite spectrum has two
791 other spectral features in the IR—a weak band centered near 980 cm^{-1} and a stronger, broader
792 band with a minimum near 425 cm^{-1} (Fig. 9). The position and relative strength of these two
793 bands are somewhat consistent with synthetic $Fe(OH)_2$ (a brucite-type Fe oxyhydroxide) (Lutz et
794 al., 1994) although their exact band positions differ, perhaps due to the presence of Ni and P in
795 this natural specimen. The OH emission peak of this tochilinite is also at a slightly longer
796 wavelength (2.79 µm) compared to synthetic $Fe(OH)_2$ (2.76 µm) (Lutz et al., 1994). In
797 summary, the longer OH/H_2O band emissivity maximum (> 2.71 µm) among our least altered
798 CM chondrites may be influenced not only by the presence of Fe-bearing phyllosilicate, but also
799 tochilinite, where these phases are commonly intergrown (forming TCIs) in these meteorites.
800 Such intergrowths likely contribute to the lack of a strong correlation of the OH/H_2O band
801 maximum with degree of aqueous alteration (Fig. 3G-H) because tochilinite abundance has not
802 been reported to vary in a predictable way with alteration. A similar conclusion was reached by
803 Nakamura et al. (2017), who observed an imperfect correlation between the OH/H_2O band
804 position and CM petrologic subtype. This study also reported a peak position of 2.79 µm for a
805 TCI (i.e., not pure tochilinite) grain in CM 2.4 DNG 06004 (spectrum not shown in that work).
806 While previous studies have also found that the maximum (or minimum in reflectance;
807 hereafter referred to as 'peak' for simplicity) of the OH/H_2O band shifts to longer wavelength
808 (smaller wavenumbers) with decreasing degree of alteration or hydration among the CMs (Beck

et al., 2010; Takir et al., 2013; Garenne et al., 2016; Nakamura et al., 2017; Bates et al., 2020), the position of the measured peak varies, even for the same meteorite. For example, the OH/H_2O band peak of CM Murchison has been estimated at 2.76 µm (this study), ~2.78 (Miyamoto, 1992), ~2.8 µm (Calvin and King, 1997; Garenne et al., 2016), and 2.82 µm (Bates et al., 2020) . And, in general, the peak positions measured among CMs in this study are at slightly shorter wavelengths than in previous studies (Fig. 10). Takir et al. (2013) found peak positions between 2.72 and 2.78 µm for petrologic subtype 2.0–2.2 (cf. this study 2.71 µm), and for subtypes ≥ 2.3, the peaks were from 2.77 to 2.80 µm (cf. this study 2.71–2.76 µm). Other reflectance studies [IR transmission data cannot be compared directly as the spectral band positions and shapes will likely be different (Salisbury, 1993; Post and Borer, 2000)] have also found generally longer wavelength positions for CM OH/H_2O band peaks: ~2.8 µm for CM 2.4/5 Murray and CM 2.5 Murchison (Calvin and King, 1997); >~2.80 µm for CMs as low as subtype 2.3 (Beck et al., 2018); and > ~2.75 µm for all CMs (2.0 to 2.6) (Garenne et al., 2016).

All of these studies collected reflectance spectra on powdered samples rather than in thin section, and therefore the longer wavelength positions of the band could be caused by particle size differences (e.g., volume vs. surface scattering) or adsorbed water effects. An early study by Miyamoto (1987) examined particle size effects on the OH/H_2O band of Murchison and found that the band depth increased and the peak shifted to longer wavelengths with decreasing particle size, but hypothesized that atmospheric water contamination, rather than particle size effects [i.e., increase in volume scattering due to decreased grain size (e.g., Salisbury, 1993)] could be the cause. Spectral heating studies by Beck et al. (2010) and Takir et al. (2013) confirmed that the OH/H_2O band depth decreases and the peak location can move to shorter wavelengths with heating (i.e., removal of adsorbed water), and so these and later spectral studies heated the

powders (typically to ~150-300°C) to minimize this effect (Garenne et al., 2016; Bates et al., 2020). Because our spectra still have a shorter wavelength peak compared to these heated powders (Fig 10), it is unclear whether there is still a residual adsorbed water effect or a real difference in wavelength position due to scattering effects. There are only two other studies that have collected FTIR spectra of phyllosilicate-bearing materials in thin section. Unfortunately, the Murchison section measured by King et al. (2018) was contaminated by terrestrial water, as evidenced by a molecular water band near 1630 cm^{-1} (compared to our sections which apart from CI Alais and WIS 91600 show no evidence of such a band; Fig. SM2), so its OH/H_2O band peak position cannot be directly compared to those measured in this study. Moroz et al. (2006) measured a minimum of ~2.71 μm for CM 2.2 Cold Bokkeveld in thin section, which is consistent with our measured peak for CM 2.2 LEW 90500. They also measured broad bands for CM 2.3 Mighei and CM 2.4/5 Murray with minima located between ~2.71 and ~2.77 (precise location not determined).

Therefore, the (albeit limited) data collected on CMs in thin section by this study and Moroz et al. (2006) suggest that spectra of powdered CM meteorites have OH/H_2O band positions at longer wavelength positions compared to solid surfaces. A direct comparison of powdered and thin section spectra for two samples, LAP 02277 and Murchison, also suggests that the shape of the OH/H_2O band, in addition to its position, varies from that of powdered samples (Fig. 10). We could find only one study, Potin et al. (2019), that measured the OH/H_2O band of both a chip and powder (while controlling for adsorbed terrestrial water on the latter) for the same phyllosilicate-bearing sample (CM2 Mukundpura), finding that the OH/H_2O band position and shape are the same. This suggests that the OH/H_2O band shape change and position shift in thin section versus a powder (or chip) is caused by the unique observational geometry of

855 a polished thin section. It seems probable that there is a contribution from specular reflection on
856 the smooth surface of the section, but our OH/H_2O band spectra do not have an obvious
857 derivative shape typical of strong specular reflection (Moroz et al., 2006; Prinsloo et al., 2014)
858 (see also Supplemental Materials; Fig. SM1). Regardless, although our analysis and conclusions
859 regarding the OH/H_2O band remain the same, this discrepancy between thin section and
860 powdered/chip meteorite spectra suggest that the OH/H_2O band measurements in this study
861 cannot be directly compared to spectra of asteroids (e.g., Takir et al., 2015). Note that this does
862 not apply to spectra presented herein collected at longer wavelengths (> ~8 μm), as this region is
863 dominated by surface scattering (whether in thin section, chip, or coarse particulates down to ~
864 75 μm), making our reflectance spectra at these wavelengths equivalent to emissivity
865 measurements of planetary surfaces through Kirchhoff's Law (Section 2.4; Salisbury et al., 1991;
866 Salisbury, 1993; Hamilton, 2018).

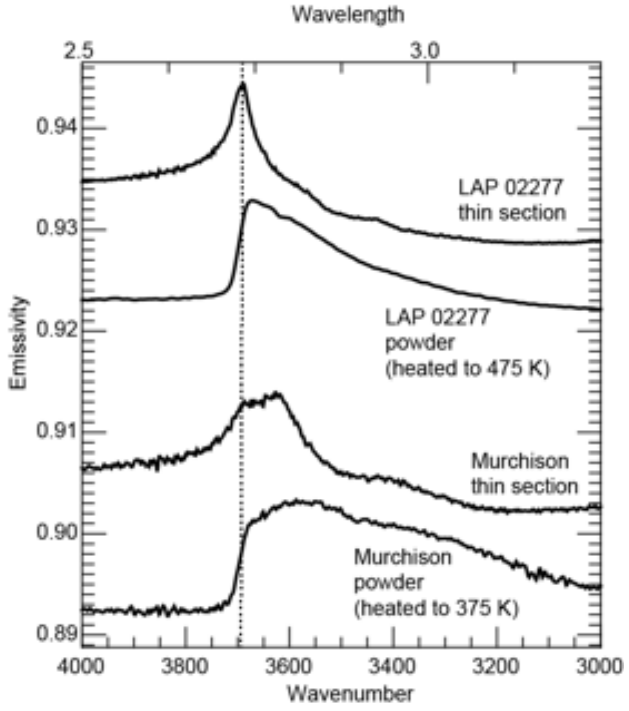

Figure 10. Comparison of powdered and thin section OH/H_2O band for two CMs. The OH/H_2O band of the thin section spectra is sharper and positioned at a slightly shorter wavelengths compared to that of the powdered samples. Dashed line marks the minimum of the LAP 02277 thin section (2.71 μm). Powdered spectra are from Takir et al. (2013; 2019) and were heated to remove adsorbed terrestrial water that contaminated the powders during sample preparation.

867

Among the heated CMs in our study, the OH/H_2O band maxima is at wavelengths ≥ 2.75 μm for all samples, and this maximum generally moves to longer wavelengths with increased degree of heating (Fig. 7 and Table 4). This is consistent with previous studies that also found OH/H_2O band peaks at longer wavelengths in thermally metamorphosed CMs than in unheated CMs (Miyamoto, 1992; Hiroi et al., 1997; Beck et al., 2018). Qualitatively, the OH/H_2O band shape of the heated CMs displays a more rounded shape than that of the unheated CMs (Fig. 8), which has also been observed by previous workers (Hiroi et al., 1996; Tonui et al., 2014; Matsuoka et al., 2017). For the weakly heated (Stage II) CMs, this shift and broadening of the OH/H_2O band could be related to the decomposition of phyllosilicate, which creates an amorphous, intermediate phase that has been well documented (Akai, 1988; Nakamura, 2005; Tonui et al., 2014). Therefore, this band could behave similarly to the Si-O stretching band for these weakly heated CMs (Section 4.1). The interpretation of the OH/H_2O band for the more highly heated CMs PCA 91008 and PCA 02010 is more complicated owing to the contamination from terrestrial weathering that has resulted in deeper than expected bands for dehydrated samples (Section 3.2.2) (Tonui et al., 2014; King et al., 2016). However, the result on the band is the same: a broadening and movement to the longer wavelengths. This suggests that the mildly heated CMs are also affected by terrestrial weathering, although we could only find mineralogical and spectral evidence of such alteration within WIS 91600 (Fig. SM2). By comparing the OH/H_2O band of heated CMs to terrestrially weathered Antarctic ordinary chondrites, Miyamoto (1992) proposed that all heated CMs are contaminated by terrestrial weathering, but their unheated, powered samples were likely also influenced by adsorbed terrestrial water.

Nakamura et al. (2017) documented movement of the OH/H_2O band center to longer wavelengths with increased heating in experimentally heated Murchison but concluded that these samples were rehydrated by atmospheric water after heating. Subsequent heating experiments that limited exposure to atmospheric water before spectral measurement showed that the band actually becomes sharper, smaller, and moves to shorter wavelength (2.72 μm when heated to 400°C) (Mogi et al., 2017). In addition, experiments investigating terrestrial chrysotile dehydration showed that the OH/H_2O band got smaller and shifted to a shorter wavelength (by 19 nm) with heating (Freund, 1974). Another experiment involving gradual heating of terrestrial lizardite confirmed that the band becomes smaller with heating (no shift noted) (McKelvy et al., 2004). Therefore, heating experiments that control for adsorbed terrestrial water demonstrate that with heating, the OH/H_2O band of serpentine (and serpentine-dominated CM Murchison) does not shift to longer wavelengths as suggested by the naturally heated CMs in our study. This could indicate that all heated CMs have been compromised by rehydration from terrestrial water, despite being bulk (non-powdered) samples. However, the bulk spectra of our unheated CM suite do not show strong evidence of such a rehydration within their OH/H_2O bands, despite similar weathering grades to the heated CMs (Tables 1–2). We can think of two possibilities for this discrepancy. First, it is possible that the heating experiments described above are not comparable to the heating conditions (e.g., duration, temperature, oxygen fugacity) experienced by naturally heated CMs. The second possibility is that dehydrated phyllosilicates are more susceptible to terrestrial rehydration. This is supported by the surface rehydration (increased emissivity at 3450 cm^{-1}) near fusion crust where phyllosilicates would have been preferentially initially dehydrated (LAP 031166, LAP 02277, PCA 91008). However, the lack of a 1630 cm^{-1} band (expect for WIS 91600; Fig. SM2) diagnostic of molecular water that would normally

indicate terrestrial hydration challenges this interpretation. Regardless, if dehydrated phyllosilicates are indeed more susceptible to rehydration from terrestrial water, particular care should be taken with samples returned from the surfaces of carbonaceous asteroids that have experienced heating and therefore may contain dehydrated phyllosilicates, such as Ryugu and Bennu (Hanna et al., 2019; Kitazato et al., 2019; Molaro et al., in revision).

4.3 Location and nature of alteration and heating within the CMs highlighted by spatially resolved FTIR

A unique aspect of our study is that we collected spectral data in thin section, in contrast to previous studies that have used powdered bulk and matrix materials; this provides spatial context for the spectral trends that we have observed among aqueously altered and heated CMs. The spectral trends at wavenumbers <1200 cm^{-1} in the unheated, aqueously altered CMs attributed to the alteration of anhydrous silicates to phyllosilicates (Section 4.1) apply primarily to the bulk samples and are not reflected in the matrix-only spectra of the samples (Fig. 2 and Tables 3–4). The strong spectral similarity of the matrix-only spectra at these wavenumbers suggests that the mineralogy of their matrices is similar, regardless of the petrologic subtype. Thus, it may be the chondrules and other inclusions (refractory inclusions, larger disaggregated anhydrous minerals) that experience the progressive alteration (of anhydrous silicates to phyllosilicates) with decreasing petrologic subtype. Garenne et al. (2014) also proposed that the relative alteration among the CMs was largely defined by the alteration of chondrules, based on thermogravimetric analysis data and the typical volume proportion of matrix within the CMs. Indeed, the Rubin et al. (2007) scales uses the relative alteration of the mafic silicates within the chondrules to distinguish among the petrologic subtypes 2.0 to 2.4.

936 The Rubin et al. (2007) scale also distinguishes among the petrologic subtypes via the
937 volume abundance and composition (‘‘FeO’’/SiO_2) of “poorly characterized phases” (now
938 referred to as TCI), which is confined to the matrix. This variation in TCI abundance and
939 composition should result in some spectral modification of the matrix-only spectra among the
940 CMs, and it does, in the shape and position of the OH/H_2O band (Fig. 2). This band probes only
941 the hydrated components [phyllosilicates and hydrated sulfides (i.e., tochilinite)], and the band
942 center of this feature in the matrix-only spectra, similar to the bulk sample spectra, moves to
943 longer wavelengths with decreasing petrologic subtype. Because this band center shift results
944 from the relative Fe/Mg composition of the phyllosilicate and tochilinite (Section 4.2), the
945 OH/H_2O band is highlighting the compositional change of the TCIs within the matrix, as
946 indicated by the Rubin et al. (2007) scale. In contrast, anhydrous silicates have bands at
947 wavenumbers <1200 cm^{-1} that overlap with those of the phyllosilicates and tochilinite (Figs. 4
948 and 9) and therefore the bulk CM spectra in this region are a combination of the matrix and
949 chondrules. Because mixing is linear in this wavenumber region (Ramsey and Christensen,
950 1998), we readily see modification of spectral features attributable to their changing proportions.
951 As the chondrules progressively alter to Fe-Mg phyllosilicates, the spectral contribution of the
952 anhydrous silicates decreases, and the bulk CM spectrum [especially for LAP 02277 (2.0) and
953 LAP 03116 (2.1)] strongly resembles that of the matrix-only spectrum that is dominated by the
954 hydrous silicates and sulfides. Thus, FTIR reveals the subtle progressive alteration of the CMs in
955 two ways: the OH/H_2O band probes the variation in abundance and composition of Mg-Fe
956 serpentine and tochilinite (the bulk of which is in the matrix, especially for higher subtypes), and
957 the wavenumber region <1200 cm^{-1} reflects the changing proportions of anhydrous silicates
958 (mainly in chondrules and larger inclusions) to Mg-Fe phyllosilicates.

959 The fact that the different FTIR wavenumber regions (OH/H_2O band at 3700-3330 cm^{-1}
960 vs. the low-wavenumber region <1200 cm^{-1}) reveal different aspects of CM aqueous alteration
961 provides some context for the differences that we noted when comparing the Rubin et al. (2007)
962 and Howard et al. (2015) scales (Section 3.1.1). By converting the Howard et al. (2015)
963 alteration scale to the Rubin et al. (2007) petrologic subtype, it appeared that our CM suite
964 showed a smaller degree of relative alteration between samples than suggested by using the latter
965 scale directly (Fig. 1). However, the Howard et al. (2015) scale uses only the proportion of
966 phyllosilicates to anhydrous silicates to classify the CMs, and therefore mainly reflects the
967 relative degree of aqueous alteration among the chondrules that is revealed via FTIR in the
968 wavenumber region <1200 cm^{-1}. However, the solid solution composition of the phyllosilicate
969 and tochilinite (TCIs) also evolves with degree of relative alteration (Tomeoka and Buseck,
970 1985) as evidenced by the variation of the OH/H_2O band among our CMs. The Rubin et al.
971 (2007) scale captures this subtle compositional variation. Therefore, because the Howard et al.
972 (2015) classification scheme does not take into account the compositional changes that occur
973 with increasing alteration, it appears less sensitive to the degree of relative aqueous alteration
974 within the CM class.
975 The spectral differences between the bulk and matrix-only spectra of the heated CMs also
976 provide information regarding the location of heating within the samples. Similar to the
977 aqueously altered CMs, spectral features <1200 cm^{-1} differ substantively between bulk and
978 matrix-only spectra for all but the most highly heated CM (PCA 02010). But for the heated
979 CMs, the matrix-only spectra display differences between the different heating stages, suggesting
980 that the matrix is being considerably modified by the thermal metamorphism. Between Stage II
981 and III matrix-only spectra, several spectral changes occur that arise from the formation of

secondary Fe-bearing olivine and pyroxene within the matrices of CMs with heating (Nakamura et al., 2000; Nakamura, 2005; Tonui et al., 2014). In particular, for Stage III PCA 91008, the 588 cm^{-1} band indicative of Fe-bearing olivine is present only in the matrix spectrum. This indicates that the Fe-bearing olivine that formed with heating is located primarily within the matrix. This concentration of thermal effects within CM matrices is consistent with petrographic observations both in this study (Section 3.2.1; Fig. 6) and previous studies (e.g., Nakamura, 2005; Tonui et al., 2014).

4.4 WIS 91600: CM or CI(-like)?

Finally, our spatially resolved spectral analysis of heated WIS 91600 highlights the uniqueness of this heated 'CM' chondrite. The matrix-only spectrum of WIS 91600 is more similar to CI Alais in Si-O stretching band shape and location than to any bulk or matrix-only CM spectrum (Figs. 2 and 7). In particular, its Si-O stretching band minima is at a high wavenumber (1001 cm^{-1}) and has a low band symmetry (0.42), similar to that of CI Alais (1008 cm^{-1} and 0.40, respectively; Tables 3–4). The wavenumber location of their Si-O bending band minima also matches within uncertainty. Because the presence of chondrules precludes its classification as a CI, it is intriguing that when isolating the matrix of WIS 91600, it spectrally (and thus chemically and mineralogically) resembles one. Tonui et al. (2014) described the matrix of WIS 91600 as CI-like and found that its bulk oxygen isotopes placed it in the field of non-heated CIs [see also Choe et al. (2010)]. Hiroi et al. (2005) noted spectral similarities in the 3 μm (OH/H_2O) band region between WIS 91600 and CI Orgueil. Other workers have noted similarities between WIS 91600 and Tagish Lake based on spectroscopic, mineralogic, isotopic, and organic evidence (Hiroi et al., 2005; Yabuta et al., 2010; Yamanobe et al., 2018).

Apart from a low abundance of olivine (10.1%) and pyroxene (1.5%), the modal mineralogy of WIS 91600 matches that of CI Alais, with high phyllosilicate (76.3%; X-ray amorphous) followed by significant magnetite (7.8%) and Fe sulfide (3.7%) (Table 2). Because the matrix-only FTIR spectrum of WIS 91600 at <1200 cm^{-1} is similar to that of CI Alais, we can interpret that its matrix is likewise dominated by phyllosilicate with lesser magnetite and Fe sulfide, with no detectable spectral contributions from anhydrous silicates. Therefore, the Si-O stretching and bending regions of the matrix-only spectrum are the spectral signature of the amorphous phyllosilicate, which, because its spectral signature is broadly similar, appears to be structurally and chemically similar to the CI Alais phyllosilicate. However, there are subtle, but important, spectral differences between them. First, the Si-O stretching region of WIS 91600 matrix is broader than that of CI Alais, with a slightly lower wavenumber minimum. Second, the OH/H_2O band of WIS 91600 is broader and at a lower wavenumber than that of CI Alais. These differences are consistent with spectral modifications due to phyllosilicate dehydration and dehydroxylation, but unlike for the mildly heated CMs EET 96029 and EET 87522, the pre-heated phyllosilicate in WIS 91600 appears to be similar to that of a CI (e.g., intergrown saponite and serpentine) rather than the pure serpentine that dominates the CMs (e.g., Zolensky et al., 1993). Tonui et al. (2014) observed flakes of dehydrated saponite with transmission electron microscopy, and the matrix phyllosilicate compositions plotted between smectite (e.g., saponite) and serpentine on an Fe-Si-Mg ternary diagram. Therefore, we hypothesize that the pre-heated matrix mineralogy (especially the structure and composition of its phyllosilicate) of WIS 91600 was very similar to that of a CI, and that mildly heated CIs may have a spectral signature similar to the matrix-only spectrum of WIS 91600. An alternative explanation for the CI-like mineralogy of WIS 91600 matrix is that post-heating aqueous alteration of initially CM-type

mineralogy (i.e., dominated by serpentine) took place and resulted in a CI-like matrix mineralogy. More work is needed to distinguish between these two scenarios.

5. Conclusions

We have characterized the IR spectra of a suite of CM chondrites that record a variety of degrees of both aqueous alteration and heating. We find spectral variations that are directly correlated to these processes.

1. The spectral variations among unheated CMs are controlled by the mineralogical and compositional changes as ferromagnesian silicates are progressively altered to Mg-rich serpentine. The strongest, most highly correlated spectral trend with degree of aqueous alteration (i.e., petrographic subtype) is the separation of the CF and Si-O stretching band minimum (R^2=0.90), although the position of the CF and the Si-O bending minimum are also significantly correlated (R^2=0.82 for both). The depth of the Mg-OH band also systematically increases (R^2=0.87) with alteration.
2. Weakly heated CMs (Stage II) exhibit spectral features due to dehydration and dehydroxylation of phyllosilicates that have formed an intermediate phase identified by previous workers (e.g., Akai, 1988). These features are broadening of the Si-O stretching band, a short wavenumber movement of its band minimum, and the disappearance of the Mg-OH band.
3. The spectra of extensively heated CMs (≥ Stage III) are distinct from that of unheated and mildly heated CMs and are dominated by secondary, Fe-bearing olivine and pyroxene.

4. The OH/H_2O band emissivity peak associated with OH^- moves to longer wavelengths with decreasing alteration, but the correlation is not strong. All moderately to highly altered CMs (≤ 2.3) have a 2.71 μm maximum. Mildly aqueously altered CMs (≥ 2.5) have wider OH/H_2O bands with a complex shape that results from contributions of Fe-bearing serpentine and tochilinite.
5. The OH/H_2O of heated CMs is broad and rounded with a peak at longer wavelengths (≥ 2.75) compared to that of unheated CMs. However, this band may be contaminated by terrestrial alteration, or heating experiments to date are not replicating natural heating within the CMs, especially for very mild heating.
6. Our study confirms that thermal metamorphism effects, especially for mild degrees of heating, are concentrated within the matrix. The matrix of WIS 91600 had a CI-like mineralogy prior to heating and may be spectrally similar to a heated CI chondrite.

These documented spectral trends can be used to characterize the relative degree of aqueous alteration and heating of CM material using IR spectroscopy (2–25 μm) and will be helpful in the interpretation of laboratory, telescopic, and spacecraft observations of carbonaceous material and asteroids.

Acknowledgements

R.D.H. was supported by the OSIRIS-REx Participating Scientist Program – Grant 80NSSC18K0229. V.E.H. was partially supported by the OSIRIS-REx mission (NASA) under Contract NNM10AA11C issued through the New Frontiers Program. A.J.K. was funded by the UK Science and Technology Facilities Council (STFC) through grant ST/R000727/1. We thank

Pierre Beck and an anonymous reviewer for insightful comments that improved our manuscript. We thank James Maner, Phil Orlandini, and Tom Etzel for their assistance during acquisition of electron beam data collection. U.S. Antarctic meteorite samples are recovered by the Antarctic Search for Meteorites (ANSMET) program which has been funded by NSF and NASA, and characterized and curated by the Department of Mineral Sciences of the Smithsonian Institution and Astromaterials Curation Office at NASA Johnson Space Center. Many thanks to the Meteorite Working Group and the Astromaterials Acquisition and Curation Office for their time and effort in getting ANSMET sample requests processed efficiently. We thank Phil Bland for the loan of CI Alais and Driss Takir for providing spectra for Figure 10. Thanks also to the Smithsonian National Museum of Natural History, curator Tim McCoy, and collection manager Julie Hoskin for the extended loan of Murchison USNM 5487, which we continually find new ways to study. Thanks to Alice Praet for sharing MATLAB code for calculating band parameters, to Deanne Rogers for useful discussions regarding band indices, and to Hannah Kaplan and Tim Glotch for insights into the behavior of the OH/H_2O and organics spectral bands in thin section. We thank the OSIRIS-REx mission editor Catherine Wolner for help in preparing this manuscript for publication and Harold Connolly Jr. for edits and suggestions which improved the quality of the manuscript.

Data Availability

Laboratory spectral data are deposited in the spectral library hosted by the Arizona State University (http://speclib.mars.asu.edu/).

References

Aines R. D. and Rossman G. R. (1984) Water in minerals? A peak in the infrared. *J. Geophys. Res.* **89**, 4059-4071.

Akai J. (1988) Incompletely transformed serpentine-type phyllosilicates in the matrix of Antarctic CM chondrites. *Geochim. Cosmoch. Acta* **52**, 1593-1599.

Alexander C. M. O. D., Fogel M., Yabuta H. and Cody G. D. (2007) The origin and evolution of chondrites recorded in the elemental and isotopic compositions of their macromolecular organic matter. *Geochim. Cosmoch. Acta* **71**, 4380-4403.

Alexander C. M. O. D., Howard K. T., Bowden R. and Fogel M. L. (2013) The classification of CM and CR chondrites using bulk H, C and N abundances and isotopic compositions. *Geochim. Cosmoch. Acta* **123**, 244-260.

Bates H. C., King A. J., Donaldson Hanna K. L., Bowles N. E. and Russell S. S. (2020) Linking mineralogy and spectroscopy of highly aqueously altered CM and CI carbonaceous chondrites in preparation for primitive asteroid sample return. *Meteoritics & Planetary Science* **55**, 77-101.

Beck P., Garenne A., Quirico E., Bonal L., Montes-Hernandez G., Moynier F. and Schmitt B. (2014) Transmission infrared spectra (2–25μm) of carbonaceous chondrites (CI, CM, CV–CK, CR, C2 ungrouped): Mineralogy, water, and asteroidal processes. *Icarus* **229**, 263-277.

Beck P., Maturilli A., Garenne A., Vernazza P., Helbert J., Quirico E. and Schmitt B. J. I. (2018) What is controlling the reflectance spectra (0.35–150 μm) of hydrated (and dehydrated) carbonaceous chondrites? *Icarus* **313**, 124-138.

Beck P., Quirico E., Montes-Hernandez G., Bonal L., Bollard J., Orthous-Daunay F.-R., Howard K. T., Schmitt B., Brissaud O., Deschamps F., Wunder B. and Guillot S. (2010) Hydrous mineralogy of CM and CI chondrites from infrared spectroscopy and their relationship with low albedo asteroids. *Geochim. Cosmoch. Acta* **74**, 4881-4892.

Bland P., Zolensky M., Benedix G. and Sephton M. (2006) Weathering of chondritic meteorites. *Meteorites and the early solar system II*, 853-867.

Brearley A. J. (2004). *A Unique Style of Alteration of Iron-Nickel Metal in WIS91600, an Unusual C2 Carbonaceous Chondrite*, Lunar and Planetary Science Conference, p. 1358.

Browning L. B., McSween H. Y., Jr. and Zolensky M. E. (1996) Correlated alteration effects in CM carbonaceous chondrites. *Geochim. Cosmoch. Acta* **60**, 2621-2633.

Brucato J. R., Strazzulla G., Baratta G. and Colangeli L. J. A. (2004) Forsterite amorphisation by ion irradiation: Monitoring by infrared spectroscopy. **413**, 395-401.

Brunetto R., Lantz C., Dionnet Z., Borondics F., Aléon-Toppani A., Baklouti D., Barucci M. A., Binzel R. P., Djouadi Z., Kitazato K. and Pilorget C. (2018) Hyperspectral FTIR imaging of irradiated carbonaceous meteorites. *Planetary and Space Science* **158**, 38-45.

Burns R. G. and Huggins F. E. (1972) Cation determinative curves for Mg-Fe-Mn olivines from vibrational spectra. *American Mineralogist* **57**, 967-985.

Calvin W. M. and King T. V. V. (1997) Spectral characteristics of iron-bearing phyllosilicates: Comparison to Orgueil (CI1), Murchison and Murray (CM2). *Meteoritics & Planetary Science* **32**, 693-701.

Choe W. H., Huber H., Rubin A. E., Kallemeyn G. W. and Wasson J. T. (2010) Compositions and taxonomy of 15 unusual carbonaceous chondrites. **45**, 531-554.

Christensen P. R., Bandfield J. L., Hamilton V. E., Howard D. A., Lane M. D., Piatek J. L., Ruff S. W. and Stefanov W. L. (2000) A thermal emission spectral library of rock-forming minerals. *J. Geophys. Res.* **105**, 9735-9739.

Christensen P. R., Hamilton V. E., Mehall G. L., Pelham D., O'Donnell W., Anwar S., Bowles H., Chase S., Fahlgren J., Farkas Z., Fisher T., James O., Kubik I., Lazbin I., Miner M., Rassas M., Schulze L., Shamordola K., Tourville T., West G., Woodward R. and Lauretta D. (2018). *The OSIRIS-REx Thermal Emission Spectrometer (OTES) Instrument*, Space Science Reviews, p. 87.

Cloutis E. A., Craig M. A., Kruzelecky R. V., Jamroz W. R., Scott A., Hawthorne F. C. and Mertzman S. A. (2008) Spectral reflectance properties of minerals exposed to simulated Mars surface conditions. *Icarus* **195**, 140-168.

Cloutis E. A., Hudon P., Hiroi T. and Gaffey M. J. (2012) Spectral reflectance properties of carbonaceous chondrites 4: Aqueously altered and thermally metamorphosed meteorites. *Icarus* **220**, 586-617.

Cloutis E. A., Hudon P., Hiroi T., Gaffey M. J. and Mann P. (2011) Spectral reflectance properties of carbonaceous chondrites: 2. CM chondrites. *Icarus* **216**, 309-346.

DellaGiustina D., Emery J., Golish D., Rozitis B., Bennett C., Burke K., Ballouz R., Becker K., Christensen P., Drouet d'Aubigny C., Hamilton V., Reuter D., Rizk B., Simon A., Asphaug E., Bandfield J., Barnouin O., Barucci M., Bierhaus E. and Bernacki M. (2019) Properties of rubble-pile asteroid (101955) Bennu from OSIRIS-REx imaging and thermal analysis. *Nature Astronomy* **3**, 341-351.

Demyk K., d'Hendecourt L., Leroux H., Jones A. P. and Borg J. (2004) IR spectroscopic study of olivine, enstatite and diopside irradiated with low energy H+ and He+ ions. *Astronomy and Astrophysics* **420**, 233-243.

Dlugogorski B. Z. and Balucan R. D. (2014) Dehydroxylation of serpentine minerals: Implications for mineral carbonation. *Renewable and Sustainable Energy Reviews* **31**, 353-367.

Donaldson Hanna K. L., Schrader D. L., Cloutis E. A., Cody G. D., King A. J., McCoy T. J., Applin D. M., Mann J. P., Bowles N. E., Brucato J. R., Connolly H. C., Dotto E., Keller L. P., Lim L. F., Clark B. E., Hamilton V. E., Lantz C., Lauretta D. S., Russell S. S. and Schofield P. F.

(2019) Spectral characterization of analog samples in anticipation of OSIRIS-REx's arrival at Bennu: A blind test study. *Icarus* **319**, 701-723.

Drief A. and Nieto F. (1999) The effect of dry grinding on antigorite from Mulhacen, Spain. *Clays and clay Minerals* **47**, 417-424.

Duke D. A. and Stephens J. D. (1964) Infrared investigation of the olivine group minerals. *American Mineralogist* **49**, 1388-1406.

Farmer V. C. (1958) The infra-red spectra of talc, saponite, and hectorite. *Mineralogical Magazine* **31**, 829-845.

Farmer V. C. (1974) The layer silicates. In *The Infra-Red Spectra of Minerals* (ed. V.C. Farmer). Mineralogical Society, London. pp. 331-364.

Freund F. (1974) Ceramics and Thermal Transformations of Minerals. In *The Infra-Red Spectra of Minerals* (ed. V.C. Farmer). Mineralogical Society, London. pp. 465-482.

Friedrich J. M., Abreu N. M., Wolf S. F., Troiano J. M. and Stanek G. L. (2018) Redox-influenced trace element compositional differences among variably aqueously altered CM chondrites. *Geochim. Cosmoch. Acta* **237**, 1-17.

Fuchs L. H., Olsen E. and Jensen K. J. (1973) Mineralogy, mineral-chemistry, and composition of the Murchison (C2) meteorite. *Smithsonian Contributions to Earth Sciences* **10**, 39.

Gaffey M. J. (1976) Spectral reflectance characteristics of the meteorite classes. *J. Geophys. Res.* **81**, 905-920.

Gaffey M. J., Burbine T. H. and Binzel R. P. (1993a) Asteroid spectroscopy: Progress and perspectives. *Meteoritics* **28**, 161-187.

Gaffey S. J., McFadden L. A., Nash D. and Pieters C. M. (1993b) Ultraviolet, visible, and near-infrared reflectance spectroscopy: Laboratory spectra of geologic materials. In *Remote Geochemical Analysis: Elemental and Mineralogical Composition* (eds. C.M. Pieters and P.A.J. Englert). Cambridge University Press, Cambridge. pp. 43-77.

Garenne A., Beck P., Montes-Hernandez G., Brissaud O., Schmitt B., Quirico E., Bonal L., Beck C. and Howard K. T. (2016) Bidirectional reflectance spectroscopy of carbonaceous chondrites: Implications for water quantification and primary composition. *Icarus* **264**, 172-183.

Garenne A., Beck P., Montes-Hernandez G., Chiriac R., Toche F., Quirico E., Bonal L. and Schmitt B. (2014) The abundance and stability of "water" in type 1 and 2 carbonaceous chondrites (CI, CM and CR). *Geochim. Cosmoch. Acta* **137**, 93-112.

Grossman J. N. and Brearley A. J. (2010) The onset of metamorphism in ordinary and carbonaceous chondrites. *Meteoritics & Planetary Science* **40**, 87-122.

Grott M., Knollenberg J., Hamm M., Ogawa K., Jaumann R., Otto K. A., Delbo M., Michel P., Biele J., Neumann W., Knapmeyer M., Kührt E., Senshu H., Okada T., Helbert J., Maturilli A., Müller N., Hagermann A., Sakatani N., Tanaka S., Arai T., Mottola S., Tachibana S., Pelivan I., Drube L., Vincent J. B., Yano H., Pilorget C., Matz K. D., Schmitz N., Koncz A., Schröder S. E., Trauthan F., Schlotterer M., Krause C., Ho T. M. and Moussi-Soffys A. (2019) Low thermal conductivity boulder with high porosity identified on C-type asteroid (162173) Ryugu. *Nature Astronomy* **3**, 971-976.

Hamilton V. E. (2000) Thermal infrared emission spectroscopy of the pyroxene mineral series. *J. Geophys. Res.* **105**, 9701-9716.

Hamilton V. E. (2010) Thermal infrared (vibrational) spectroscopy of Mg-Fe olivines: A review and applications to determining the composition of planetary surfaces. *Chemie der Erde* **70**, 7-33, doi:10.1016/j.chemer.2009.1012.1005.

Hamilton V. E. (2018). *Spectral classification of ungrouped carbonaceous chondrites I: Data collection and processing*, Lunar and Planetary Science Conference, Houston, TX, p. 1759.

Hamilton V. E., Simon A. A., Christensen P. R., Reuter D. C., Clark B. E., Barucci M. A., Bowles N. E., Boynton W. V., Brucato J. R., Cloutis E. A., Connolly H. C., Donaldson Hanna K. L., Emery J. P., Enos H. L., Fornasier S., Haberle C. W., Hanna R. D., Howell E. S., Kaplan H. H., Keller L. P., Lantz C., Li J. Y., Lim L. F., McCoy T. J., Merlin F., Nolan M. C., Praet A., Rozitis B., Sandford S. A., Schrader D. L., Thomas C. A., Zou X. D., Lauretta D. S. and Team' t. O.-R. (2019) Evidence for widespread hydrated minerals on asteroid (101955) Bennu. *Nature Astronomy* **3**, 332-340.

Hanna R. D., Haberle C. W., Hamilton V. E., Lee M. R., King A. J., Lindgren P., Howell E. S., Molaro J. L., Kaplan H. H., Abreu N. M., Friedrich J. M. and Lauretta D. (2019) Bennu: An Aqueously Altered and Mildly Heated CM Carbonaceous Asteroid. *82nd Annual Meeting of the Meteoritical Society.*

Hanna R. D., Ketcham R. A., Zolensky M. and Behr W. (2015) Impact-induced brittle deformation, porosity loss, and aqueous alteration in the Murchison CM chondrite. *Geochim. Cosmoch. Acta* **171**, 256-282.

Harrington R. and Righter K. (2017). *Carbonaceous chondrite thin section preparation*, Lunar and Planetary Science Conference, p. 6304.

Hiroi T., Tonui E., Pieters C., Zolensky M., Ueda Y., Miyamoto M. and Sasaki S. (2005) Meteorite WIS91600: A new sample related to a D-or T-type asteroid. *Lunar and Planetary Science Conference XXXVI.* Houston, TX. #1564(abstr.).

Hiroi T., Zolensky M. and Pieters C. (1997) Characterization of unusual CI/CM/CR meteorites from reflectance spectroscopy. *Lunar and Planetary Science Conference.* #577(abstr.).

Hiroi T., Zolensky M. E., Pieters C. M. and Lipschutz M. E. (1996) Thermal metamorphism of the C, G, B, and F asteroids seen from the 0.7 μm, 3 μm, and UV absorption strengths in comparison with carbonaceous chondrites. *Meteoritics & Planetary Science* **31**, 321-327.

Howard K. T., Alexander C. M. O. D., Schrader D. L. and Dyl K. A. (2015) Classification of hydrous meteorites (CR, CM and C2 ungrouped) by phyllosilicate fraction: PSD-XRD modal mineralogy and planetesimal environments. *Geochim. Cosmoch. Acta* **149**, 206-222.

Howard K. T., Benedix G. K., Bland P. A. and Cressey G. (2009) Modal mineralogy of CM2 chondrites by X-ray diffraction (PSD-XRD). Part 1: Total phyllosilicate abundance and the degree of aqueous alteration. *Geochim. Cosmoch. Acta* **73**, 4576-4589.

Howard K. T., Benedix G. K., Bland P. A. and Cressey G. (2011) Modal mineralogy of CM chondrites by X-ray diffraction (PSD-XRD): Part 2. Degree, nature and settings of aqueous alteration. *Geochim. Cosmoch. Acta* **75**, 2735-2751.

Kaplan H. H., Milliken R. E., Alexander C. M. O. D. and Herd C. D. K. (2019) Reflectance spectroscopy of insoluble organic matter (IOM) and carbonaceous meteorites. *Meteoritics & Planetary Science* **54**, 1051-1068.

King A., Maturilli A., Schofield P. F., Helbert J. and Russell S. S. (2016) Thermal alteration of CI and CM chondrites: Links to primitive C-type asteroid surfaces. *Hayabusa Symposium.* Tokyo, Japan.

King A. J., Schofield P. F., Howard K. T. and Russell S. S. (2015) Modal mineralogy of CI and CI-like chondrites by X-ray diffraction. *Geochim. Cosmoch. Acta* **165**, 148-160.

King A. J., Schofield P. F. and Russell S. S. (2017) Type 1 aqueous alteration in CM carbonaceous chondrites: Implications for the evolution of water-rich asteroids. *Meteoritics & Planetary Science* **52**, 1197-1215.

King A. J., Schofield P. F., Stephen N. R., Frogley M. D., Cinque G. and Russell S. S. (2018) Investigating the history of volatiles in the solar system using synchrotron infrared micro-spectroscopy. *Infrared Physics & Technology* **94**, 244-249.

Kitazato K., Milliken R. E., Iwata T., Abe M., Ohtake M., Matsuura S., Arai T., Nakauchi Y., Nakamura T., Matsuoka M., Senshu H., Hirata N., Hiroi T., Pilorget C., Brunetto R., Poulet F., Riu L., Bibring J.-P., Takir D., Domingue D. L., Vilas F., Barucci M. A., Perna D., Palomba E., Galiano A., Tsumura K., Osawa T., Komatsu M., Nakato A., Arai T., Takato N., Matsunaga T., Takagi Y., Matsumoto K., Kouyama T., Yokota Y., Tatsumi E., Sakatani N., Yamamoto Y., Okada T., Sugita S., Honda R., Morota T., Kameda S., Sawada H., Honda C., Yamada M., Suzuki H., Yoshioka K., Hayakawa M., Ogawa K., Cho Y., Shirai K., Shimaki Y., Hirata N., Yamaguchi A., Ogawa N., Terui F., Yamaguchi T., Takei Y., Saiki T., Nakazawa S., Tanaka S., Yoshikawa M., Watanabe S. and Tsuda Y. (2019) The surface composition of asteroid 162173 Ryugu from Hayabusa2 near-infrared spectroscopy. eaav7432.

Koeppen W. C. and Hamilton V. E. (2008) Global distribution, composition, and abundance of olivine on the surface of Mars from thermal infrared data. *J. Geophys. Res.* **113**, doi:10.1029/2007JE002984.

Lantz C., Brunetto R., Barucci M. A., Dartois E., Duprat J., Engrand C., Godard M., Ledu D. and Quirico E. J. A. (2015) Ion irradiation of the Murchison meteorite: Visible to mid-infrared spectroscopic results. **577**, A41.

Lantz C., Brunetto R., Barucci M. A., Fornasier S., Baklouti D., Bourçois J. and Godard M. (2017) Ion irradiation of carbonaceous chondrites: A new view of space weathering on primitive asteroids. *Icarus* **285**, 43-57.

Lauretta D. S., Hua X. and Buseck P. R. (2000) Mineralogy of fine-grained rims in the ALH 81002 CM chondrite. *Geochim. Cosmoch. Acta* **64**, 3263-3273.

Lee M. R., Lindgren P., King A. J., Greenwood R. C., Franchi I. A. and Sparkes R. (2016) Elephant Moraine 96029, a very mildly aqueously altered and heated CM carbonaceous chondrite: Implications for the drivers of parent body processing. *Geochim. Cosmoch. Acta* **187**, 237-259.

Leroux H., Cuvillier P., Zanda B. and Hewins R. H. (2015) GEMS-like material in the matrix of the Paris meteorite and the early stages of alteration of CM chondrites. *Geochim. Cosmoch. Acta* **170**, 247-265.

Lipschutz M. E., Zolensky M. E. and Bell M. S. J. A. M. R. (1999) New petrographic and trace element data on thermally metamorphosed carbonaceous chondrites. *Antarctic Meteorite Research* **12**, 57-80.

Lutz H. D., Möller H. and Schmidt M. (1994) Lattice vibration spectra. Part LXXXII. Brucite-type hydroxides M(OH)2 (M = Ca, Mn, Co, Fe, Cd) — IR and Raman spectra, neutron diffraction of Fe(OH)2. *Journal of Molecular Structure* **328**, 121-132.

Lyon R. J. P. (1964). *Evaluation of infrared spectrophotometry for compositional analysis of lunar and planetary soils, II, Rough and powdered surfaces*. Stanford Research Institute, Palo Alto, CA, p. 175.

Mackinnon I. D. R. and Zolensky M. E. (1984) Proposed structures for poorly characterized phases in C2M carbonaceous chondrite meteorites. *Nature* **309**, 240-242.

Mason E., King A., Bates H., Schofield P., Donaldson-Hanna K., Bowles N. and Russell S. (2018) Tracing The Earliest Stages of Hydrothermal Alteration on Primitive Asteroids. *Lunary and Planetary Science Conference.* Houston, TX. #1482(abstr.).

Matsuoka M., Nakamura T., Miyajima N., Imae N., Yamaguchi A. and Kojima H. (2017) Vis-IR reflectance spectroscopy of hydrous carbonaceous chondrites with variable heating and dehydration degrees. *Lunar and Planetary Science Conference.*

McAdam M. M., Sunshine J. M., Howard K. T. and McCoy T. M. (2015) Aqueous alteration on asteroids: Linking the mineralogy and spectroscopy of CM and CI chondrites. *Icarus* **245**, 320-332.

McKelvy M. J., Chizmeshya A. V. G., Diefenbacher J., Béarat H. and Wolf G. (2004) Exploration of the Role of Heat Activation in Enhancing Serpentine Carbon Sequestration Reactions. *Environmental Science & Technology* **38**, 6897-6903.

Michalski J. R., Kraft M. D., Sharp T. G., Williams L. B. and Christensen P. R. (2006) Emission spectroscopy of clay minerals and evidence for poorly crystalline aluminosilicates on Mars from Thermal Emission Spectrometer data. *J. Geophys. Res.* **11**, DOI:10.1029/2005JE002438.

Miyamoto M. (1987) Infrared diffuse reflectances (2.5-25 μm) of some meteorites. *Icarus* **70**, 146-152.

Miyamoto M. (1992) Infrared diffuse reflectance spectra of several thermally metamorphosed carbonaceous chondrites. *Proceedings of the NIPR Symposium on Antarctic Meteorites* **5**, 155-164.

Mogi K., Yamashita S., Nakamura T., Matsuoka M., Okumura S. and Furukawa Y. (2017) Dehydration Process of Experimentally Heated Murchison Without any Effects of Adsorbed and Rehydrated Water. *80th Annual Meeting of the Meteoritical Society.*

Molaro J. L., Walsh K. J., Jawin E. R., Ballouz R.-L., Bennett C. A., Golish D. R., d'Aubigny C. D., DellaGuistina D. N., Rizk B., Schwartz S. R., Delbo M., Hanna R. D., Pajola M., Campins H., Ryan A. J., Bottke W. F. and Lauretta D. S. (in revision) In Situ Evidence of Thermally Induced Rock Breakdown Widespread on Bennu's Surface. *Nature Communications*.

Moroz L. V., Schmidt M., Schade U., Hiroi T. and Ivanova M. A. (2006) Synchrotron-based infrared microspectroscopy as a useful tool to study hydration states of meteorite constituents. *Meteoritics & Planet. Sci.* **41**, 1219-1230.

Nakamura T. (2005) Post-hydration thermal metamorphism of carbonaceous chondrites. *Journal of Mineralogical and Petrological Sciences* **100**, 260-272.

Nakamura T., Kitajima F. and Takaoka N. (2000) Thermal metamorphism of CM carbonaceous chondrites deduced from phyllosilicate decomposition and trapped noble gas abundance. *Antarctic Meteorites XXV.* #102-105(abstr.).

Nakamura T., Matsuoka M., Yamashita S., Sato Y., Mogi K., Enokido Y., Nakata A., Okumura S., Furukawa Y. and Zolensky M. (2017) Mineralogical, Spectral, and Compositional Changes During Heating of Hydrous Carbonaceous Chondrites. *Lunar and Planetary Science Conference.*

Nakato A., Brearley A., Nakamura T., Noguchi T., Ahn I., Lee J., Matsuoka M. and Sasaki S. J. L. P. S. (2013) PCA 02012: A unique thermally metamorphosed carbonaceous chondrite. *Lunar and Planetary Science Conference XLIV.* Houston, TX. #2708(abstr.).

Nakato A., Nakamura T. and Noguchi T. (2009) Mineralogical and chemical variations recorded in dehydrated carbonaceous chondrites. *72nd Annual Meteoritical Society Meeting.* Nancy, France. #5336(abstr.).

Okada T., Fukuhara T., Tanaka S., Taguchi M., Arai T., Sakatani N., Shimaki Y., Senshu H., Ogawa Y. and Demura H. (2019) Thermal Imaging of C-Type Near Earth Asteroid 162173 Ryugu by Thermal Imfrared Imager TIR on Hayabusa2. *Lunar and Planetary Science Conference.* #1325(abstr.).

Post J. L. and Borer L. (2000) High-resolution infrared spectra, physical properties, and micromorphology of serpentines. *Applied Clay Science* **16**, 73-85.

Potin S., Beck P., Schmitt B. and Moynier F. (2019) Some things special about NEAs: Geometric and environmental effects on the optical signatures of hydration. *Icarus* **333**, 415-428.

Prinsloo L. C., Wadley L. and Lombard M. (2014) Infrared reflectance spectroscopy as an analytical technique for the study of residues on stone tools: potential and challenges. *Journal of Archaeological Science* **41**, 732-739.

Quirico E., Bonal L., Beck P., Alexander C. M. O. D., Yabuta H., Nakamura T., Nakato A., Flandinet L., Montagnac G., Schmitt-Kopplin P. and Herd C. D. K. (2018) Prevalence and nature of heating processes in CM and C2-ungrouped chondrites as revealed by insoluble organic matter. *Geochim. Cosmoch. Acta* **241**, 17-37.

Quirico E., Orthous-Daunay F.-R., Beck P., Bonal L., Brunetto R., Dartois E., Pino T., Montagnac G., Rouzaud J.-N., Engrand C. and Duprat J. (2014) Origin of insoluble organic matter in type 1 and 2 chondrites: New clues, new questions. *Geochim. Cosmoch. Acta* **136**, 80-99.

Ramsey M. S. and Christensen P. R. (1998) Mineral abundance determination: Quantitative deconvolution of thermal emission spectra. *J. Geophys. Res.* **103**, 577-596.

Rossman G. R. (1988) Vibrational spectroscopy of hydrous components. *Reviews in Mineralogy and Geochemistry* **18**, 193-206.

Rubin A. E., Trigo-Rodriguez J. M., Huber H. and Wasson J. T. (2007) Progressive aqueous alteration of CM carbonaceous chondrites. *Geochim. Cosmoch. Acta* **71**, 2361-2382.

Salisbury J. W. (1993) Mid-infrared spectroscopy: Laboratory data. In *Remote Geochemical Analysis: Elemental and Mineraliogical Composition* (eds. C.M. Pieters and P.A.J. Englert). Cambridge University Press, New York. pp. 79-98 (Ch. 74).

Salisbury J. W. and Walter L. S. (1989) Thermal infrared (2.5-13.5 μm) spectroscopic remote sensing of igneous rock types on particulate planetary surfaces. *J. Geophys. Res.* **94**, 9192-9202.

Salisbury J. W., Walter L. S. and Vergo N. (1987) Mid-infrared (2.1-25 μm) spectra of minerals: First Edition. *U.S.G.S., Open File Report*, 87-263.

Salisbury J. W., Walter L. S., Vergo N. and D'Aria D. M. (1991) *Infrared (2.1 - 25 um) Spectra of Minerals*. Johns Hopkins University Press, Baltimore, MD.

Sandford S. A. (1984) Infrared transmission spectra from 2.5 to 25 μm of various meteorite classes. *Icarus* **60**, 115-126.

Sato K., MIyamoto M. and Zolensky M. E. (1997) Absorption bands near three micrometers in diffuse reflectance spectra of carbonaceous chondrites: Comparison with asteroids. *Meteoritics & Planetary Science* **32**, 503-507.

Takir D., Emery J. P. and McSween H. Y. (2015) Toward an understanding of phyllosilicate mineralogy in the outer main asteroid belt. *Icarus* **257**, 185-193.

Takir D., Emery J. P., McSween J. H. Y., Hibbitts C. A., Clark R. N., Pearson N. and Wang A. (2013) Nature and degree of aqueous alteration in CM and CI carbonaceous chondrites. *Meteoritics & Planet. Sci.*, 1618-1637.

Takir D., Stockstill-Cahill K. R., Hibbitts C. A. and Nakauchi Y. (2019) 3-μm reflectance spectroscopy of carbonaceous chondrites under asteroid-like conditions. *Icarus* **333**, 243-251.

Tomeoka K. and Buseck P. R. (1985) Indicators of aqueous alteration in CM carbonaceous chondrites: Microtextures of a layered mineral containing Fe, S, O and Ni. *Geochim. Cosmoch. Acta* **49**, 2149-2163.

Tomeoka K., McSween Jr H. Y. and Buseck P. R. (1989) Mineralogical alteration of CM carbonaceous chondrites: A review. *Proc. NIPR Symp. Antarct. Meteorites.* #221-234(abstr.).

Tonui E., Zolensky M., Hiroi T., Nakamura T., Lipschutz M. E., Wang M.-S. and Okudaira K. (2014) Petrographic, chemical and spectroscopic evidence for thermal metamorphism in carbonaceous chondrites I: CI and CM chondrites. *Geochim. Cosmoch. Acta* **126**, 284-306.

Vincent R. K. and Hunt G. R. (1968) Infrared reflectance from mat surfaces. *Applied Optics* **7**, 53-59.

Yabuta H., Alexander C. M. O. D., Fogel M. L., Kilcoyne A. L. D. and Cody G. D. (2010) A molecular and isotopic study of the macromolecular organic matter of the ungrouped C2 WIS 91600 and its relationship to Tagish Lake and PCA 91008. **45**, 1446-1460.

Yamanobe M., Nakamura T. and Nakashima D. (2018) Oxygen isotope reservoirs in the outer asteroid belt inferred from oxygen isotope systematics of chondrule olivines and isolated forsterite and olivine grains in Tagish Lake-type carbonaceous chondrites, WIS 91600 and MET 00432. *Polar Science* **15**, 29-38.

Zolensky M., Barrett R. and Browning L. (1993) Mineralogy and composition of matrix and chondrule rims in carbonaceous chondrites. *Geochim. Cosmoch. Acta* **57**, 3123-3148.

Zolensky M. E., Mittlefehldt D. W., Lipschutz M. E., Wang M.-S., Clayton R. N., Mayeda T. K., Grady M. M., Pillinger C. and Barber D. (1997) CM chondrites exhibit the complete petrologic range from type 2 to 1. *Geochim. Cosmoch. Acta* **61**, 5099.